Supplemental Information

Long-Term Implant Fibrosis Prevention in Rodents and Non-Human Primates Using Localized Deliverable Crystals

Shady Farah[1,2,3]*, Joshua C. Doloff[1,2,3,12]*, Peter Müller[4], Atieh Sadraei[1], Hye Jung Han[1,3], Katy Olafson[1,2,3,5], Keval Vyas[1], Hok Hei Tam[1,3], Jennifer Hollister-Locke[6], Piotr S. Kowalski[1,2], Marissa Griffin[1], Ashley Meng[1], Malia McAvoy[1,7], Adam C. Graham[8], James McGarrigle[9], Jose Oberholzer[9], Gordon C. Weir[6], Dale L. Greiner[10], Robert Langer[1,2,3,7,11], and Daniel G. Anderson[1,2,3,7,11#]

1. David H Koch Institute for Integrative Cancer Research, Massachusetts Institute of Technology, 500 Main Street, Cambridge, Massachusetts 02139, USA.

2. Department of Chemical Engineering, Massachusetts Institute of Technology, 77 Massachusetts Avenue, Cambridge, Massachusetts 02139, USA.

3. Department of Anesthesiology, Boston Children's Hospital, Harvard Medical School, 300 Longwood Ave, Boston, Massachusetts 02115, USA.

4. X-Ray Diffraction Facility, MIT Department of Chemistry, Massachusetts Institute of Technology, 77 Massachusetts Avenue, Cambridge, Massachusetts 02139, USA.

5. Department of Chemical and Biomolecular Engineering, University of Houston, Houston, TX 77204

6. Section on Islet Cell and Regenerative Biology, Research Division, Joslin Diabetes Center, One Joslin Place, Boston, MA 02215, USA.

7. Harvard-MIT Division of Health Science Technology, Massachusetts Institute of Technology, 77 Massachusetts Avenue, Cambridge, MA, 02139, USA

8. Center for Nanoscale Systems, Harvard University, Cambridge, MA, USA.

9. Department of Surgery, Division of Transplantation, University of Illinois at Chicago, 840 S. Wood Street, Chicago, IL 60612, USA.

10. Program in Molecular Medicine, University of Massachusetts Medical School, Worcester, MA 01605, USA

11. Institute for Medical Engineering and Science, Massachusetts Institute of Technology, 77 Massachusetts Avenue, Cambridge, Massachusetts 02139, USA.

12. Present address: Departments of Biomedical & Materials Science Engineering, Translational Tissue Engineering Center, Wilmer Eye Institute & the Institute for NanoBioTechnology Johns Hopkins University School of Medicine, Baltimore, MD 21231, USA.

*: Equal contributing authors.

#email: dgander@mit.edu; Tel.: +1 617 258 6843; fax: +1 617 258 8827.

1. Supplementary Figures:

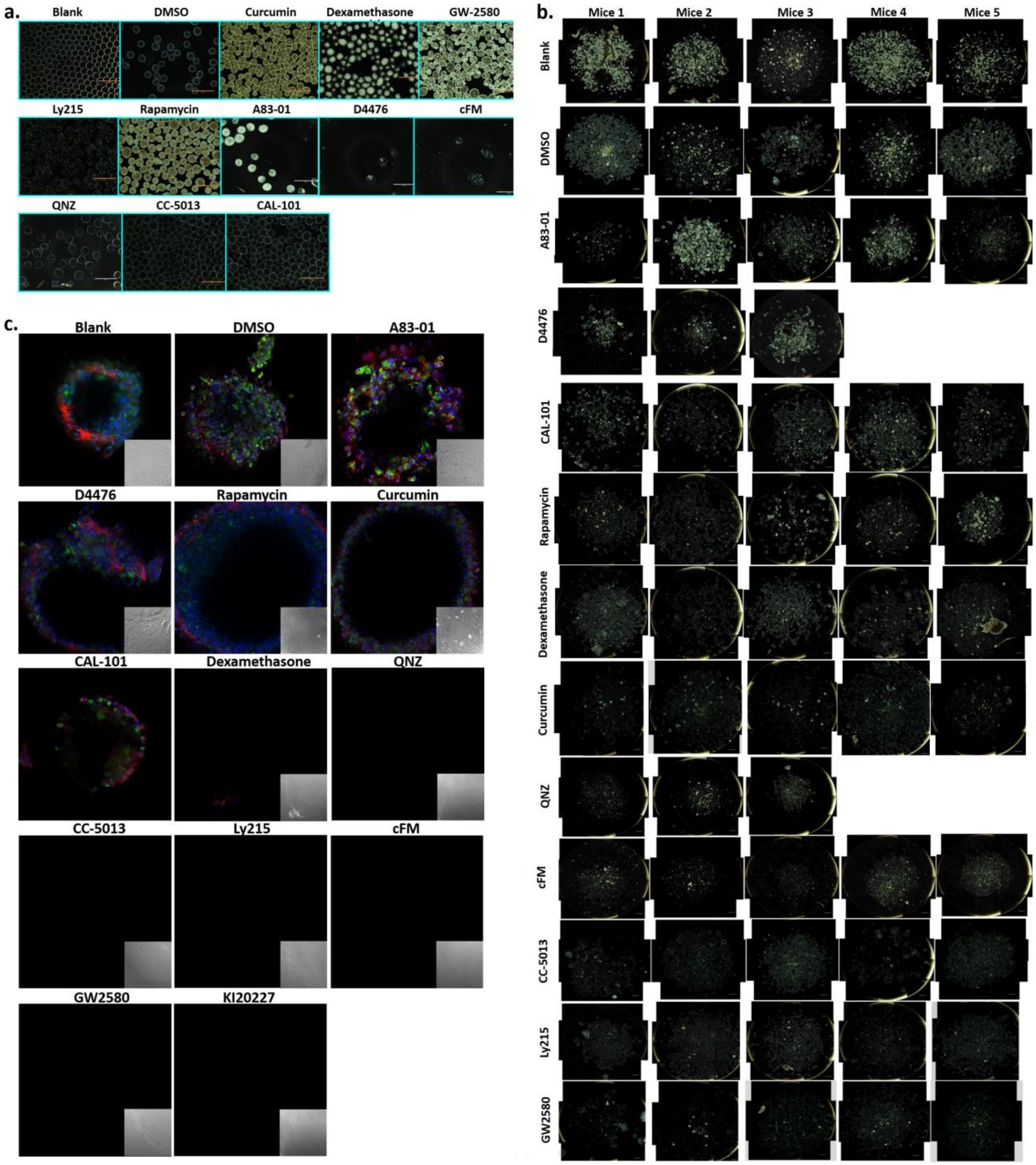

Supplemental Figure 1. **Additional in vivo characterization of amorphous drug screen – a**) Alginate capsule appearance following encapsulation of various amorphous drug treatment groups, as indicated, and retrieved 2 weeks post-IP implantation in C57BL/6 mice (corresponding to those used for screening in Fig. 1). **b**) Complete panel of phase contrast images of all retrieved encapsulated amorphous-formulated drug (at 5 mg drug/ml alginate) groups following 2-week intraperitoneal implantations (IP). Images obtained from n = 5/group, except in the cases of QNZ and D4476, due to some drug toxicity issues. QNZ dose was reduced for later testing at 0.1 mg/ml, (D4476 was ultimately not pursued). The same material volume (500 µL) of hydrogel spheres was implanted into each mouse in all cases. **c**) Confocal microscopy images showing reduced or no fibrotic overgrowth on alginate microcapsules after 2-week incubations (Blue: DAPI nuclear stain; Green: macrophage marker CD68; and Red: Fibrosis marker α-smooth muscle actin). Insets: brightfield images of the same fields of view in the main confocal panel. All subpanels reflect representative data from in vivo experiments repeated 3 times.

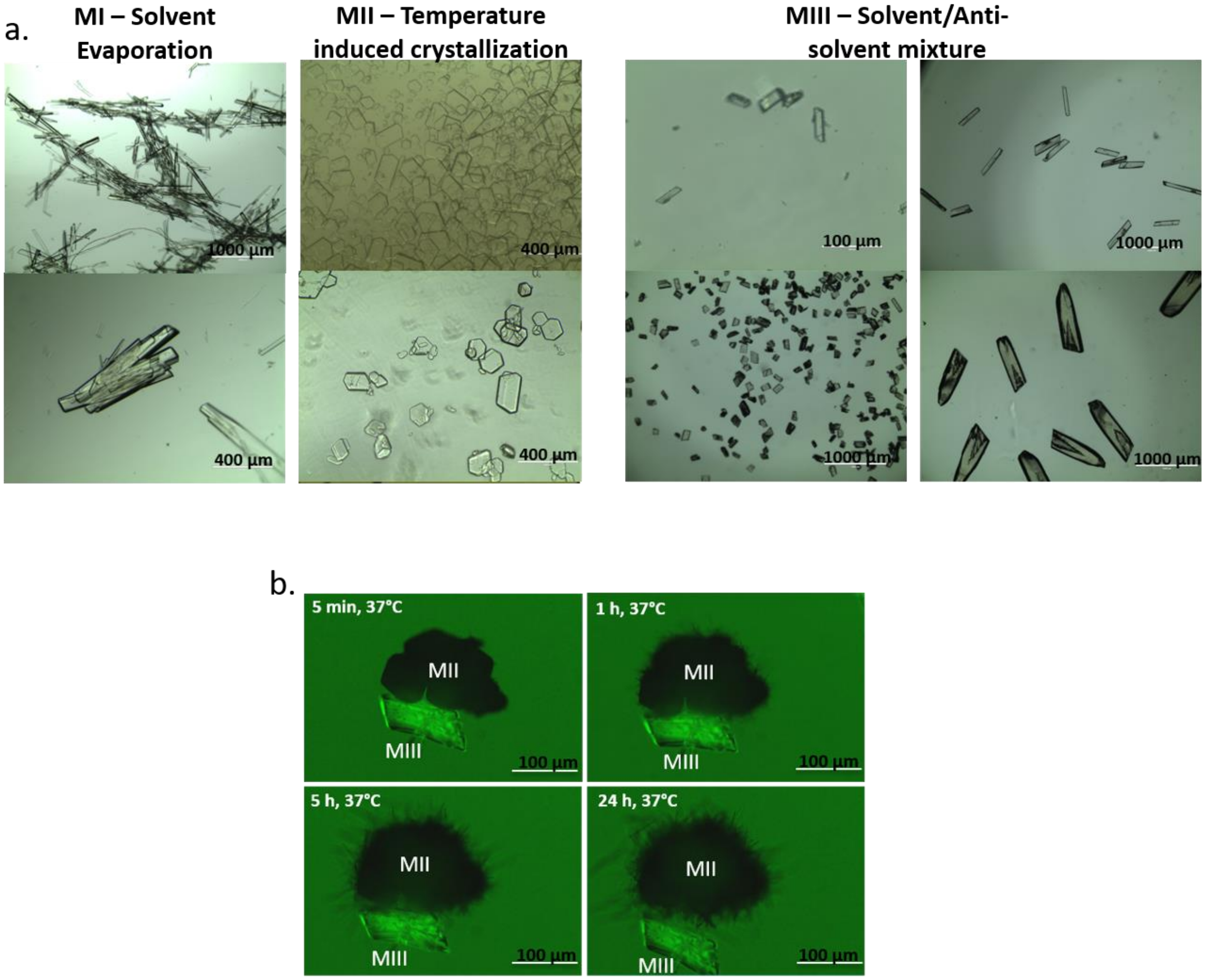

Supplemental Figure 2. **Crystal development and characterization** – **a**) Examination of 3 crystallization techniques for the drug GW2580: I-solvent evaporation, II-temperature induced crystallization and III-Solvent/anti-solvent mixture. **b**) Fluorescent microscope images of crystal stability and release under accelerated release conditions (37ºC, PBS +0.3% SDS). Blackened crystals (MII) were found to lose their structure due to bulk release, as compared to MIII crystals, which maintained their shape due to slow surface release. See Supplementary Video 1. All subpanels reflect representative data from experiments repeated 3 times.

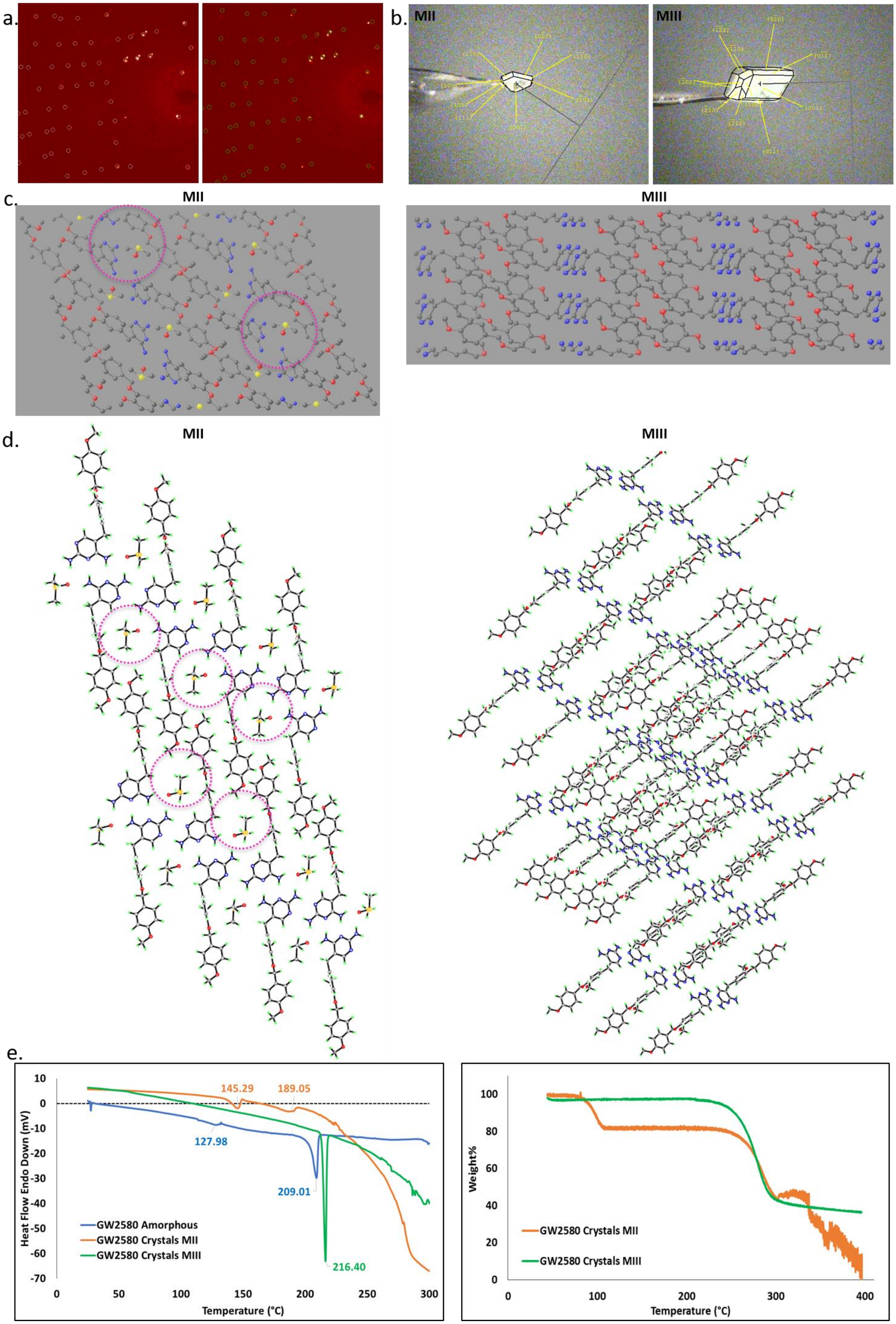
a.
b.
MII
MIII
c.
MII
MIII
d.
MII
MIII
e.
Heat Flow Endo Down (mV)
Temperature (°C)
145.29
189.05
127.98
209.01
216.40
GW2580 Amorphous
GW2580 Crystals MII
GW2580 Crystals MIII
10
0
-10
-20
-30
-40
-50
-60
-70
0
50
100
150
200
250
300
Weight%
Temperature (°C)
GW2580 Crystals MII
GW2580 Crystals MIII
100
80
60
40
20
0
0
100
200
300
400

Supplemental Figure 3. Crystalline structure, diffraction pattern and thermal stability – a) SXRD diffraction pattern images of GW2580 crystals prepared by solvent evaporation (MI) emphasizes crystal twinning marked with circles. White circles correspond to contributions from one twin domain, green circles to contributions from the other. **b**) Images of GW2580 crystals prepared by the other techniques (MII and MIII) showing the crystals mounted in SXRD with crystal face indexing, and pointing on the surface that has been studied for mechanism of release (001 or 00-1). **c**) *R*epresentative packing plot for a GW2580 crystal prepared by MII and MIII details structure properties. For MII: the 3D pattern order inside the developed crystals as revealed by SXRD analysis, at the angstrom level, exhibiting the involvement of DMSO (pink circles) in the interaction between the molecules inside the lattice. DMSO involvement affects the formation strong interaction hydrophobic and hydrogen bonds between the drug molecule's moieties and hydrogen bond bridges between the repeating units leading to less condensed crystals with non-hydrogen atom volume i.e. GW2580 18.7 A^3. For MIII: a highly compact crystalline structure identified with non-hydrogen atom volume i.e. GW2580 16.7 A^3 were maximum overlap between hydrophobic moieties while inter and intra hydrogen bonds were found to tighten and connecting crystalline structure; hydrophobic channels and interface were also identified. **d**) Representative packing plot for a crystal prepared by MII or by MIII; in both cases with GW2580, as determined by SXRD. Image presents the compact structure of the crystal layer prepared by MIII as indicated by higher density of molecules in the sheet (indicating higher packing density), determined as described in the methods and main text. In contrast MII crystal’s layers shows the presence of the solvent presence along the sheet (i.e. DMSO) which can be easily released by contact with aqueous media leading to crystals collapse and fast release. **e**) Differential scanning calorimetry (DSC) analysis: amorphous formulation was identified with a glass temperature (Tg) of 127.98°C and followed by a wide-peak melting Tm of 209.01°C, indicating partial undesired self-crystallization. In comparison, GW2580 crystals prepared by MII exhibited 2 peaks at 145.29°C and 189.05°C attributed to DMSO, followed by crystal collapse and melting, while MIII crystals were found to have a sharp Tm peak at 216.40°C. **f**) Thermogravimetric analysis (TGA): thermogravimetric curves of crystal sample mass change with temperature over the course of the pyrolysis reaction indicated a higher thermal stability of MIII crystals. MII crystals exhibited early weight loss (18.9%), close to the calculated 17.6% amount of DMSO by SXRD. All subpanels reflect representative data from experiments repeated 3 times.

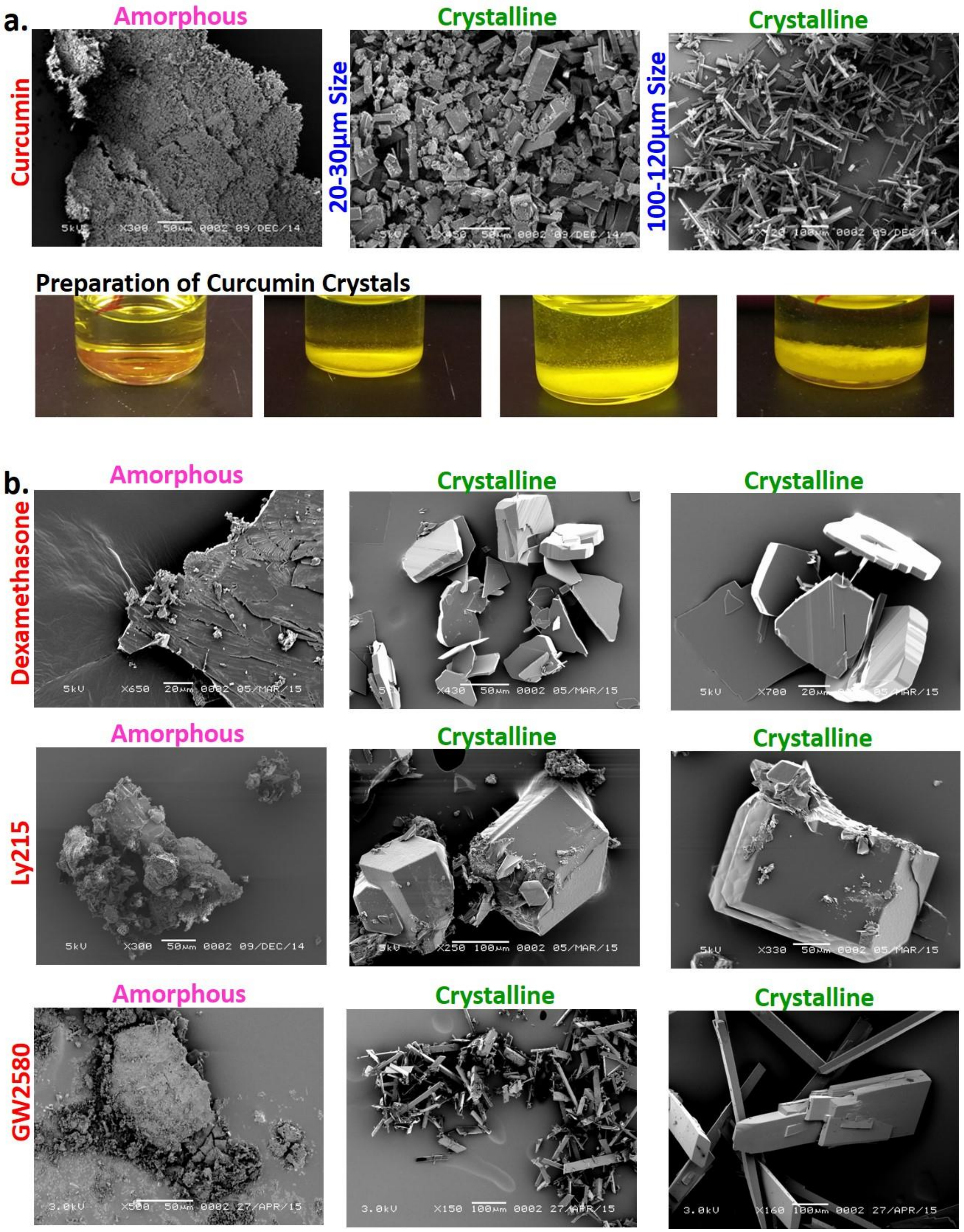

Supplemental Figure 4. Amorphous and crystalline materials preparation and SEM evaluation – a) SEM images for broad-spectrum anti-inflammatory curcumin as amorphous and two differently sized crystalline formulations, respectively, and representative photos showing crystals formation (yellow color) in liquid drug solution (i.e. solvent/anti-solvent mixture) over 4 hours. **b**) Representative SEM images confirm the difference between amorphous materials and rationally designed crystals of one classical broad-spectrum anti-inflammatory agent dexamethasone as well as two targeted agents (Ly215799, Ly215, TGFβ inhibitor; and CSF1R inhibitor GW2580) prepared as fine amorphous, small crystals, or larger tuned crystals, respectively. All subpanels reflect representative data from experiments repeated 3 times.

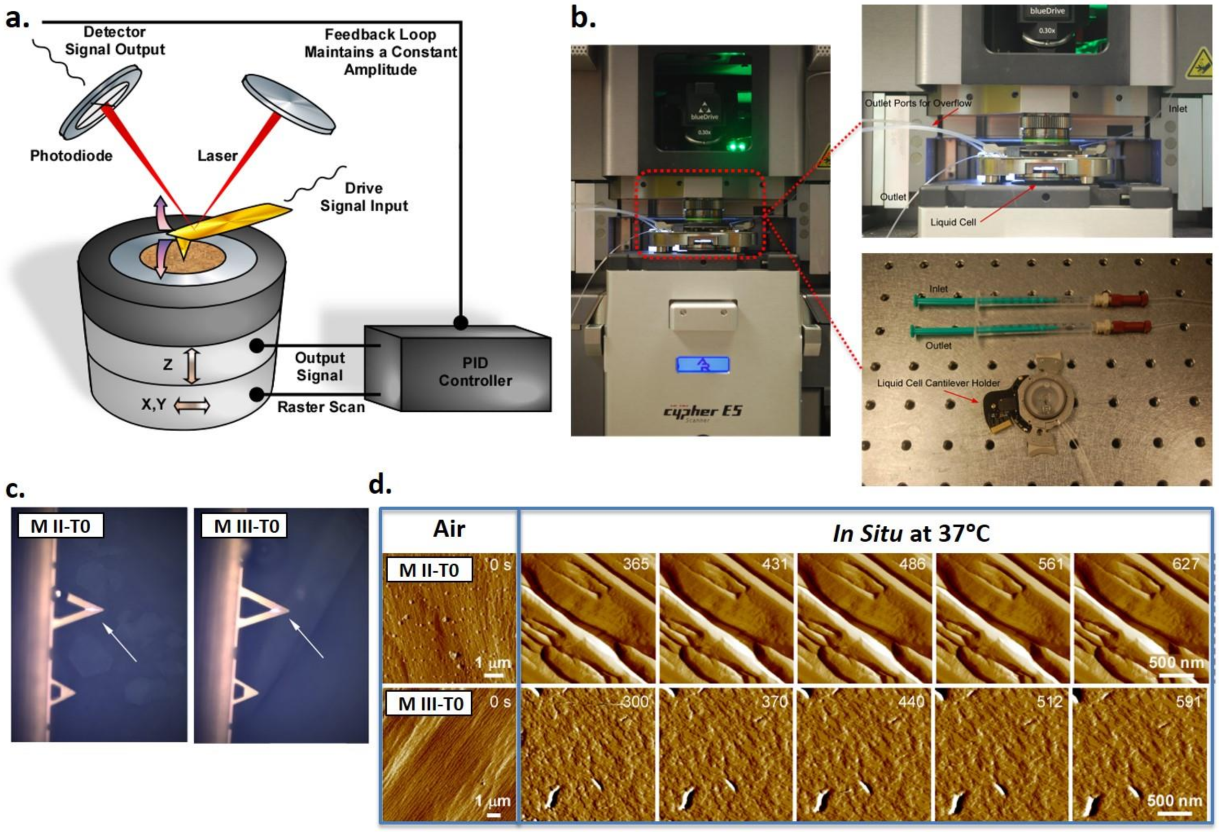

Supplemental Figure 5. *In situ* AFM set-up and analysis – a) Schematic drawing of the AFM set-up. **b**) Cypher ES Environmental AFM from Asylum Research (Santa Barbara, CA) used for all *in situ* release monitoring experiments. The photo also shows the sealed liquid cells for the Cypher AFM, with images collected in contact mode using Olympus TR800PSA probes (Silicon nitride probe, Cr/Au coated 5/30, 0.15 N/m spring constant) with tapping frequency of ca. 32 kHz. **c**) Representative microscope images pointing to the atomic force microscopy (AFM) cantilever used for measurements taken of the developed crystal surface (001). **d**) Time-resolved *in situ* atomic force microscopy (AFM) showing real-time release from GW2580 crystal surfaces in a physiologically relevant environment. MII and MIII crystals were monitored at t=0 (open to air) and starting from t=365 sec and t=300 sec respectively in PBS, 37ºC. All subpanels reflect representative data from experiments repeated 3 times.

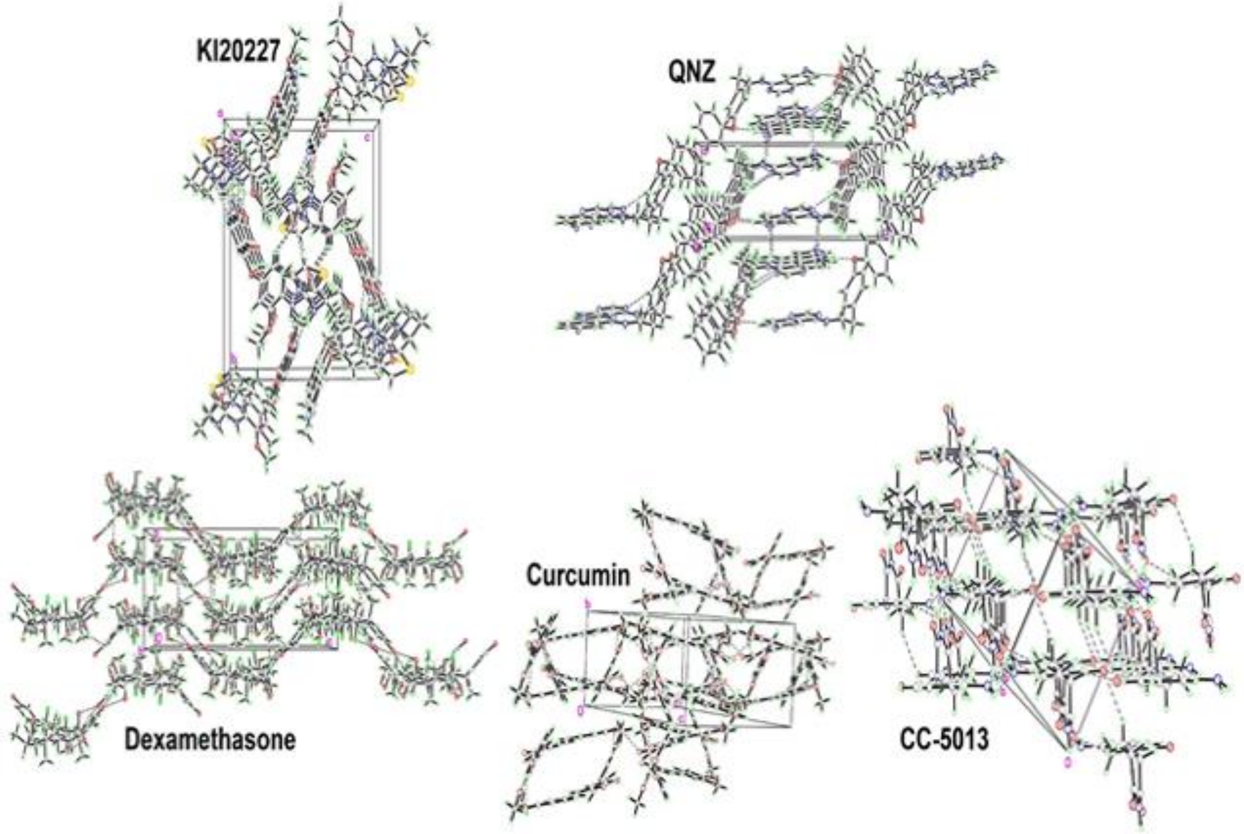

Supplemental Figure 6. Single X-ray diffraction – representative SXRD structures of two classical anti-inflammatory agents, dexamethasone and curcumin, as well as three targeted agents (CC-5013, QNZ and Ki20227). All subpanels reflect representative data from experiments repeated 3 times.

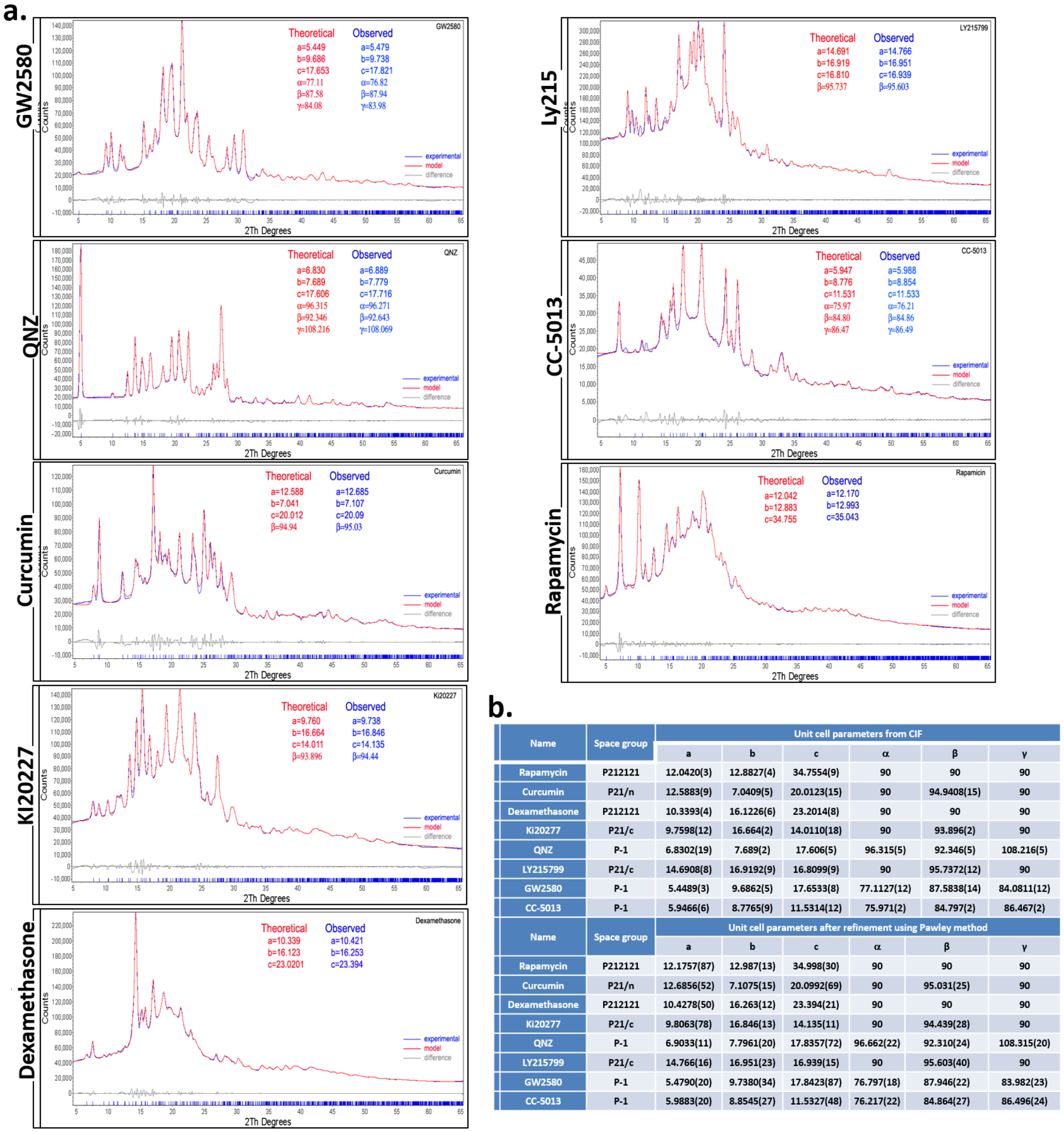

Name	Space group	Unit cell parameters from CIF					
		a	b	c	α	β	γ
Rapamycin	P212121	12.0420(3)	12.8827(4)	34.7554(9)	90	90	90
Curcumin	P21/n	12.5883(9)	7.0409(5)	20.0123(15)	90	94.9408(15)	90
Dexamethasone	P212121	10.3393(4)	16.1226(6)	23.2014(8)	90	90	90
Ki20277	P21/c	9.7598(12)	16.664(2)	14.0110(18)	90	93.896(2)	90
QNZ	P-1	6.8302(19)	7.689(2)	17.606(5)	96.315(5)	92.346(5)	108.216(5)
LY215799	P21/c	14.6908(8)	16.9192(9)	16.8099(9)	90	95.7372(12)	90
GW2580	P-1	5.4489(3)	9.6862(5)	17.6533(8)	77.1127(12)	87.5838(14)	84.0811(12)
CC-5013	P-1	5.9466(6)	8.7765(9)	11.5314(12)	75.971(2)	84.797(2)	86.467(2)
Name	**Space group**	**Unit cell parameters after refinement using Pawley method**					
		a	**b**	**c**	**α**	**β**	**γ**
Rapamycin	P212121	12.1757(87)	12.987(13)	34.998(30)	90	90	90
Curcumin	P21/n	12.6856(52)	7.1075(15)	20.0992(69)	90	95.031(25)	90
Dexamethasone	P212121	10.4278(50)	16.263(12)	23.394(21)	90	90	90
Ki20277	P21/c	9.8063(78)	16.846(13)	14.135(11)	90	94.439(28)	90
QNZ	P-1	6.9033(11)	7.7961(20)	17.8357(72)	96.662(22)	92.310(24)	108.315(20)
LY215799	P21/c	14.766(16)	16.951(23)	16.939(15)	90	95.603(40)	90
GW2580	P-1	5.4790(20)	9.7380(34)	17.8423(87)	76.797(18)	87.946(22)	83.982(23)
CC-5013	P-1	5.9883(20)	8.8545(27)	11.5327(48)	76.217(22)	84.864(27)	86.496(24)

Supplemental Figure 7. Powder X-ray diffraction – a) PXRD polymorph analysis (*red*: simulated vs. *blue*: measured) of leading candidates in the following order: GW2580, QNZ, curcumin, KI2027, dexamethasone, Ly215799, CC-5013 and rapamycin confirming a single polymorph in each case. **b)** Summary table of unit cell parameters from CIF vs. after refinement using Pawley method. All subpanels reflect representative data from experiments repeated 3 times.

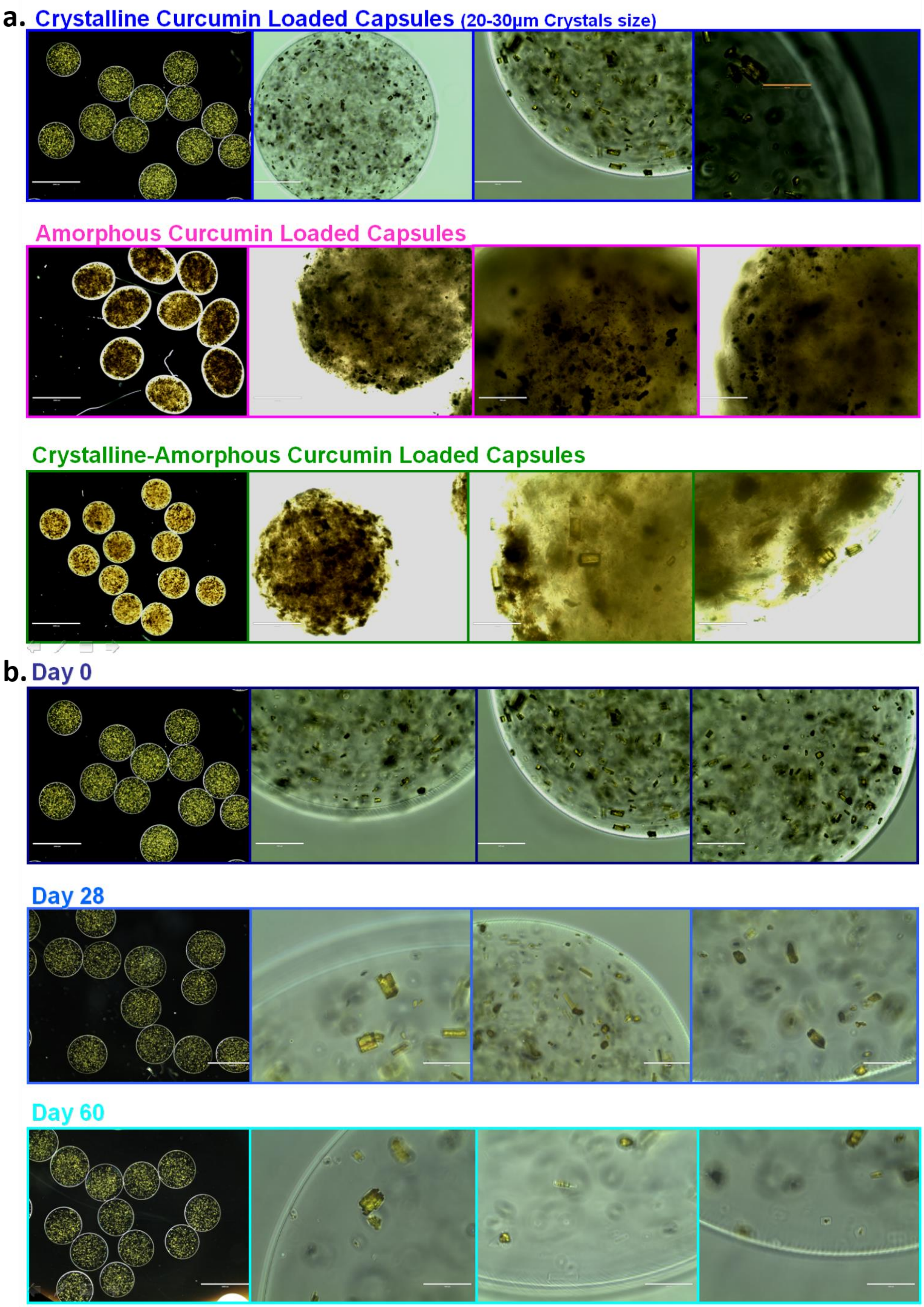
a.
Crystalline Curcumin Loaded Capsules (20-30µm Crystals size)
Amorphous Curcumin Loaded Capsules
Crystalline-Amorphous Curcumin Loaded Capsules
b.
Day 0
Day 28
Day 60

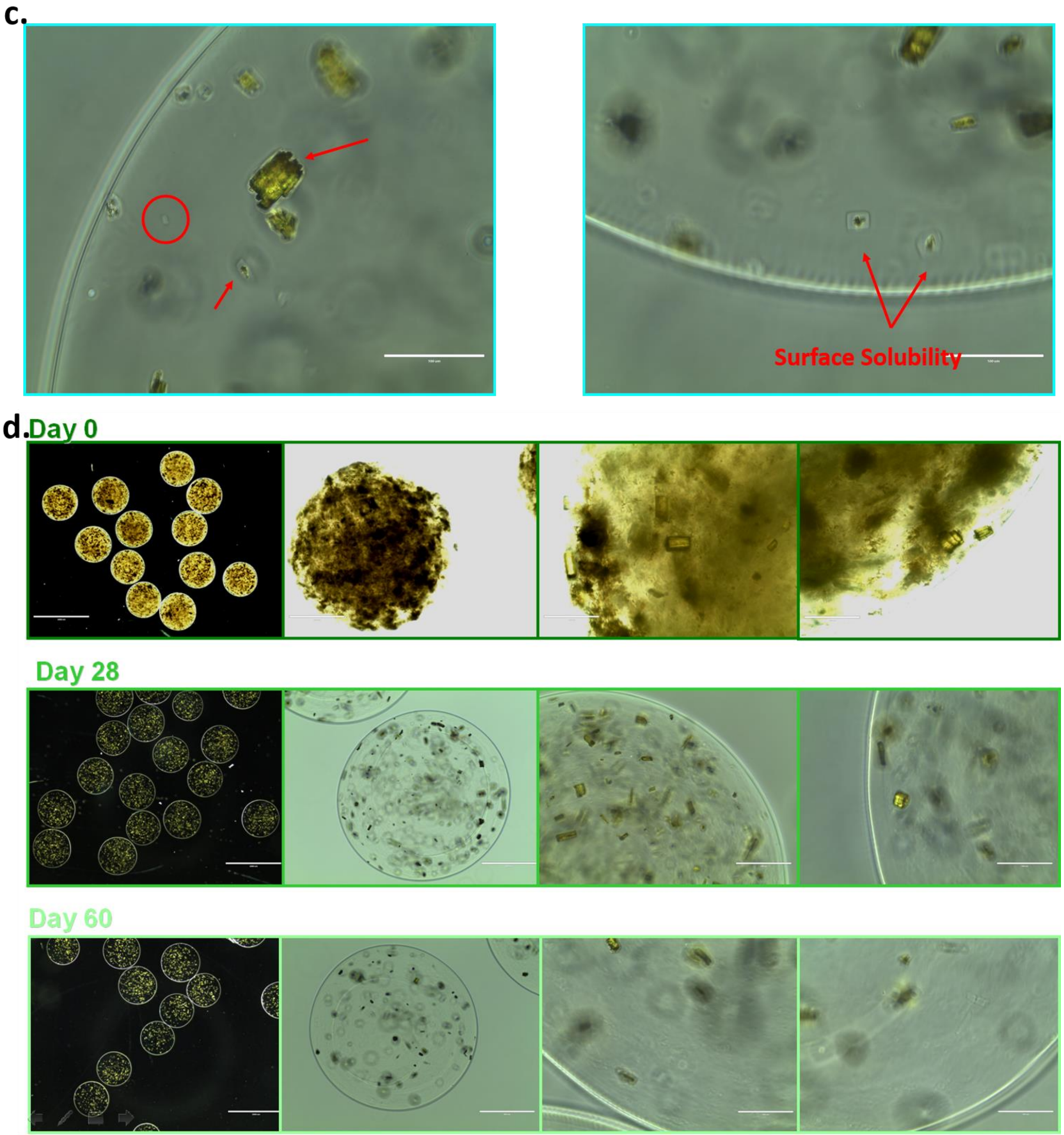
c.
Surface Solubility
d.
Day 0
Day 28
Day 60

e.

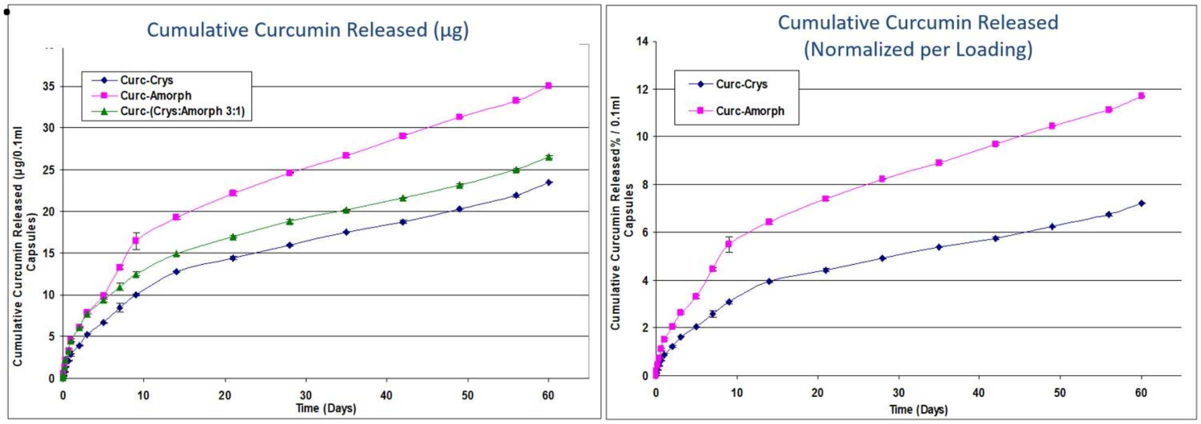

f. Crystalline QNZ Loaded Capsules

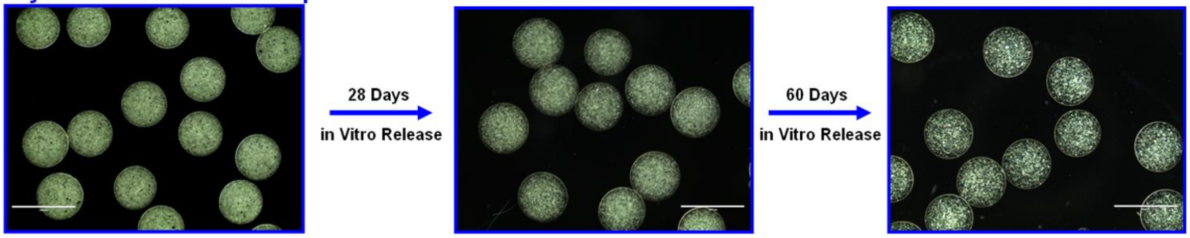

Amorphous QNZ Loaded Capsules

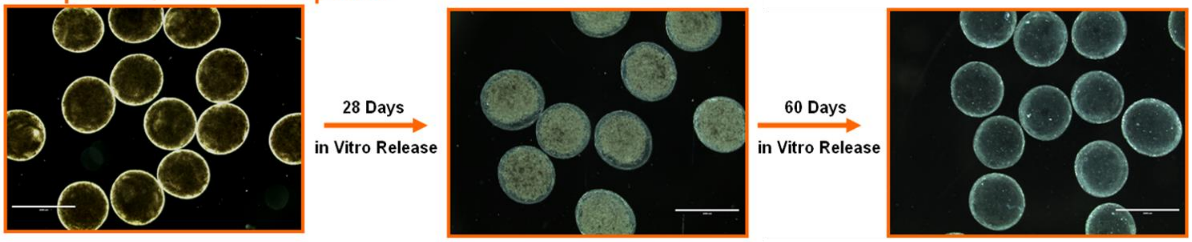

Crystalline-Amorphous QNZ Loaded Capsules

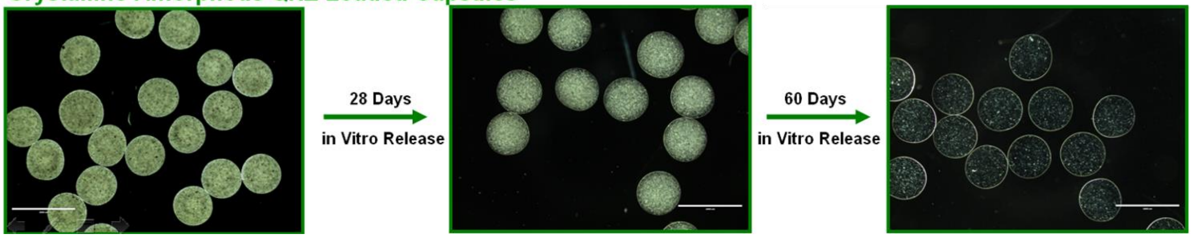

Supplemental Figure 8. Release manipulation by controlling crystallinity% in the loading dose – a) Light microscopy images of 1500 µm alginate capsules loaded with the broad-spectrum anti-inflammatory drug curcumin formulated as crystals, amorphous, or a mixed blend of amorphous and crystalline drug (1:3 respectively). **b**) Time course showing the same fields of view and capsules formulated with crystalline drugs in all cases at time zero, 28 days, or 60 days of *in vitro* release. **c**) Zoomed in images at 60 days showing examples of surface erosion/dissolution for crystalline-formulated curcumin while smaller crystals released faster than the larger crystals due to increased surface: volume ratio. **d**) Time course showing the same fields of view and capsules formulated with crystalline-amorphous mixture drugs in all cases at time zero, 28 days, or 60 days of *in vitro* release, were first the amorphous formulation (appears as cloudy yellowish background) released first while the crystalline particles remained for extended time. **e**) HPLC-quantified cumulative drug release of curcumin from capsules shown in **c** and **d**, also demonstrating tunable release rates with titering or blending amorphous and crystalline fractions (1:3 respectively). **f**) Light microscopy images of 1500 μm alginate capsules loaded with the targeted TNFα inhibitor QNZ formulated as crystals, amorphous, or a mixed blend of amorphous and crystalline drug over a period of 2 months showing the same behavior as curcumin, formulated in different states. All subpanels reflect representative data from experiments repeated 3 times.

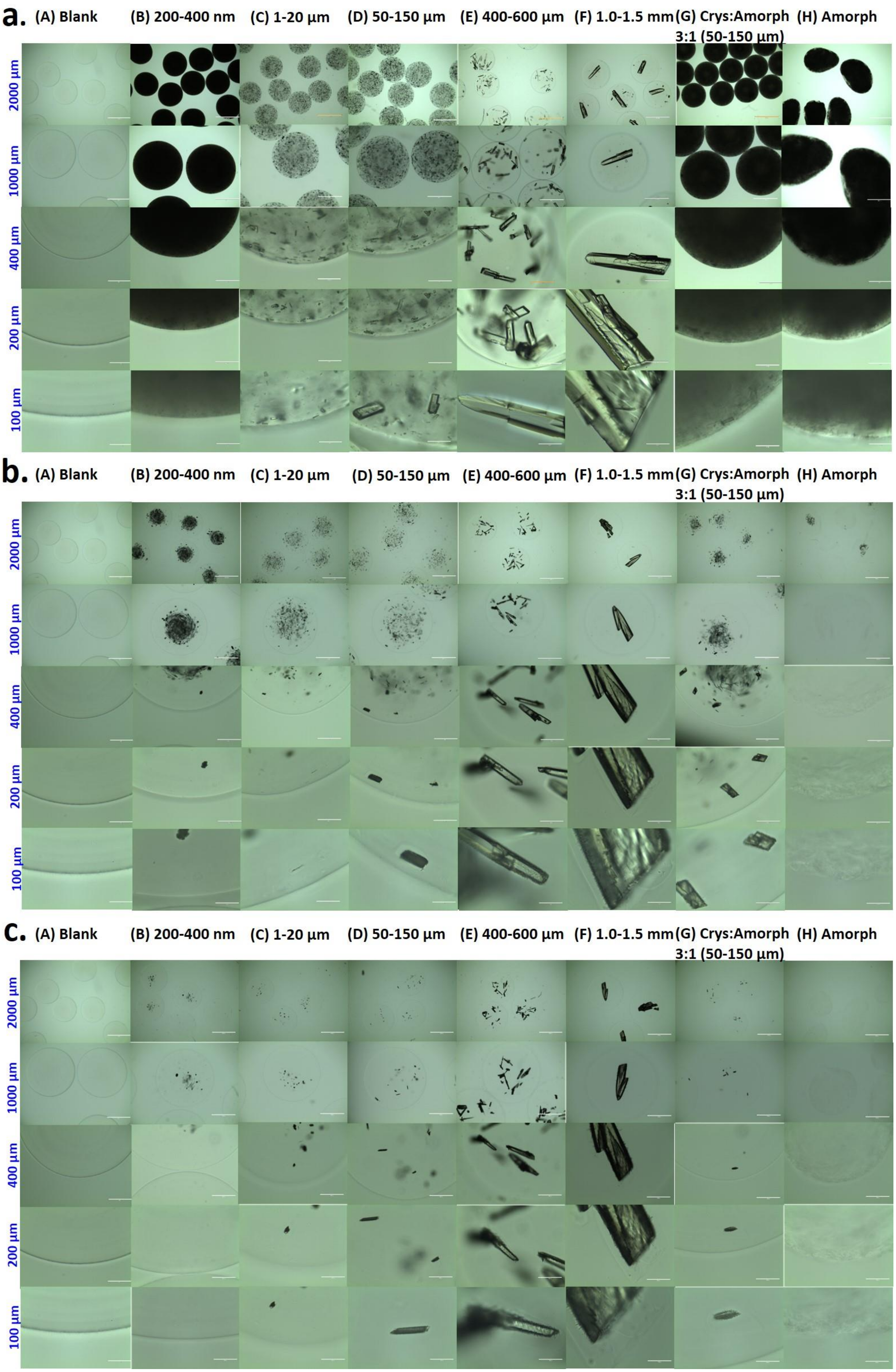
a.
(A) Blank
(B) 200-400 nm
(C) 1-20 µm
(D) 50-150 µm
(E) 400-600 µm
(F) 1.0-1.5 mm
(G) Crys:Amorph 3:1 (50-150 µm)
(H) Amorph
2000 µm
1000 µm
400 µm
200 µm
100 µm
b.
(A) Blank
(B) 200-400 nm
(C) 1-20 µm
(D) 50-150 µm
(E) 400-600 µm
(F) 1.0-1.5 mm
(G) Crys:Amorph 3:1 (50-150 µm)
(H) Amorph
2000 µm
1000 µm
400 µm
200 µm
100 µm
c.
(A) Blank
(B) 200-400 nm
(C) 1-20 µm
(D) 50-150 µm
(E) 400-600 µm
(F) 1.0-1.5 mm
(G) Crys:Amorph 3:1 (50-150 µm)
(H) Amorph
2000 µm
1000 µm
400 µm
200 µm
100 µm

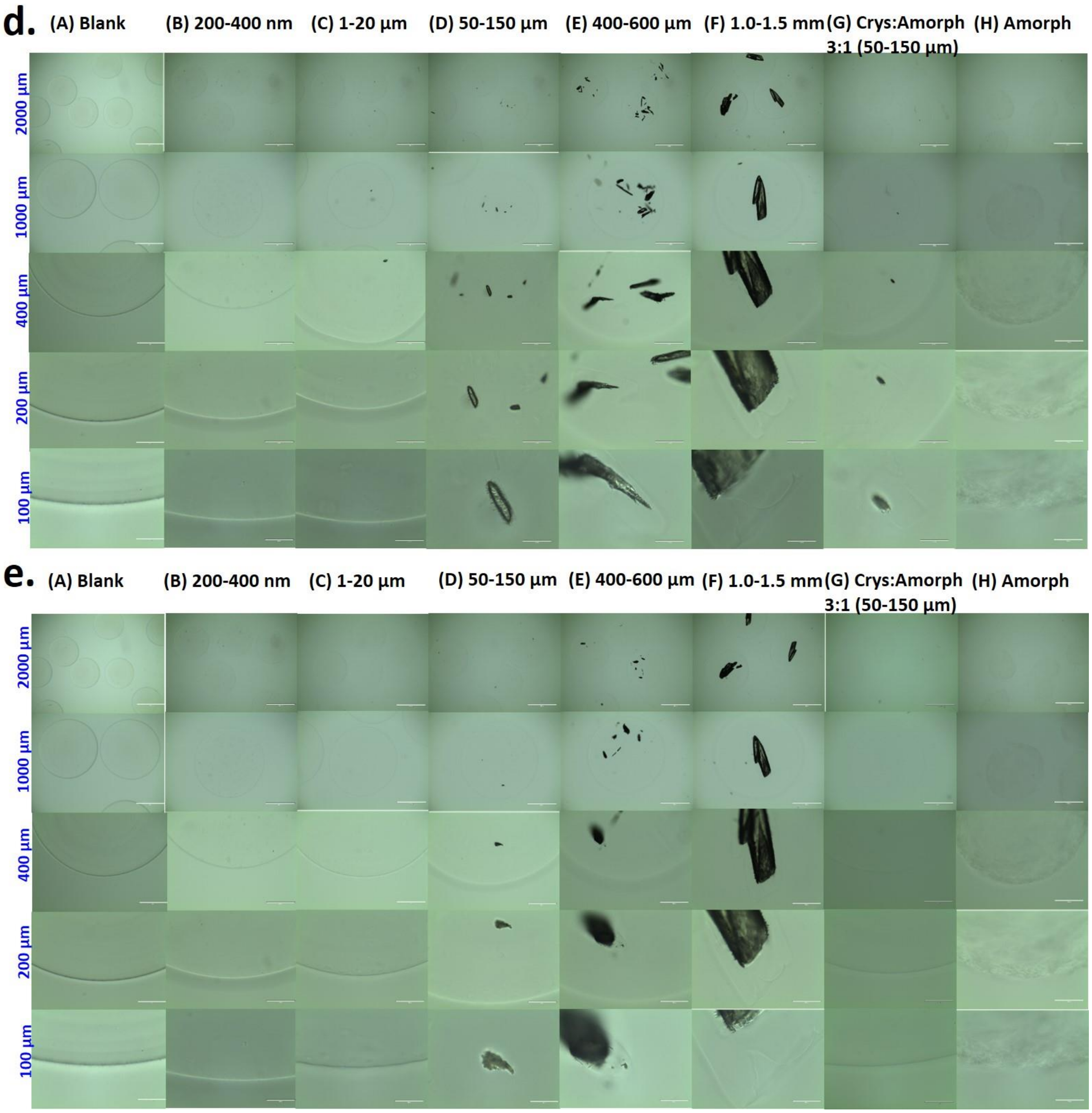

Supplemental Figure 9. Release manipulation by encapsulating different crystal size ranges and studied under accelerated release condition (37°C, PBS + 0.1% SDS)– Representative microscope photos showing slow surface erosion/dissolution and long-term release (over at least 4 weeks) for crystalline GW2580 (at small, medium, and large crystal formulation sizes) loaded into 2000 µm alginate capsules, or much faster drug diffusion and release for amorphous formulations. Smaller crystals leave behind empty spaces within the 3D alginate, whereas larger crystals remain longer exhibiting longer-term controlled surface release/erosion. Time course showing the same fields of view and capsules in all cases at time zero (**a**), 1 week (**b**), 2 weeks (**c**), 3 weeks (**d**), or 4 weeks (**e**) of accelerated *in vitro* release. Scale bar sizes, indicated in blue on the left hand side (same size for each row). All subpanels reflect representative data from experiments repeated 3 times.

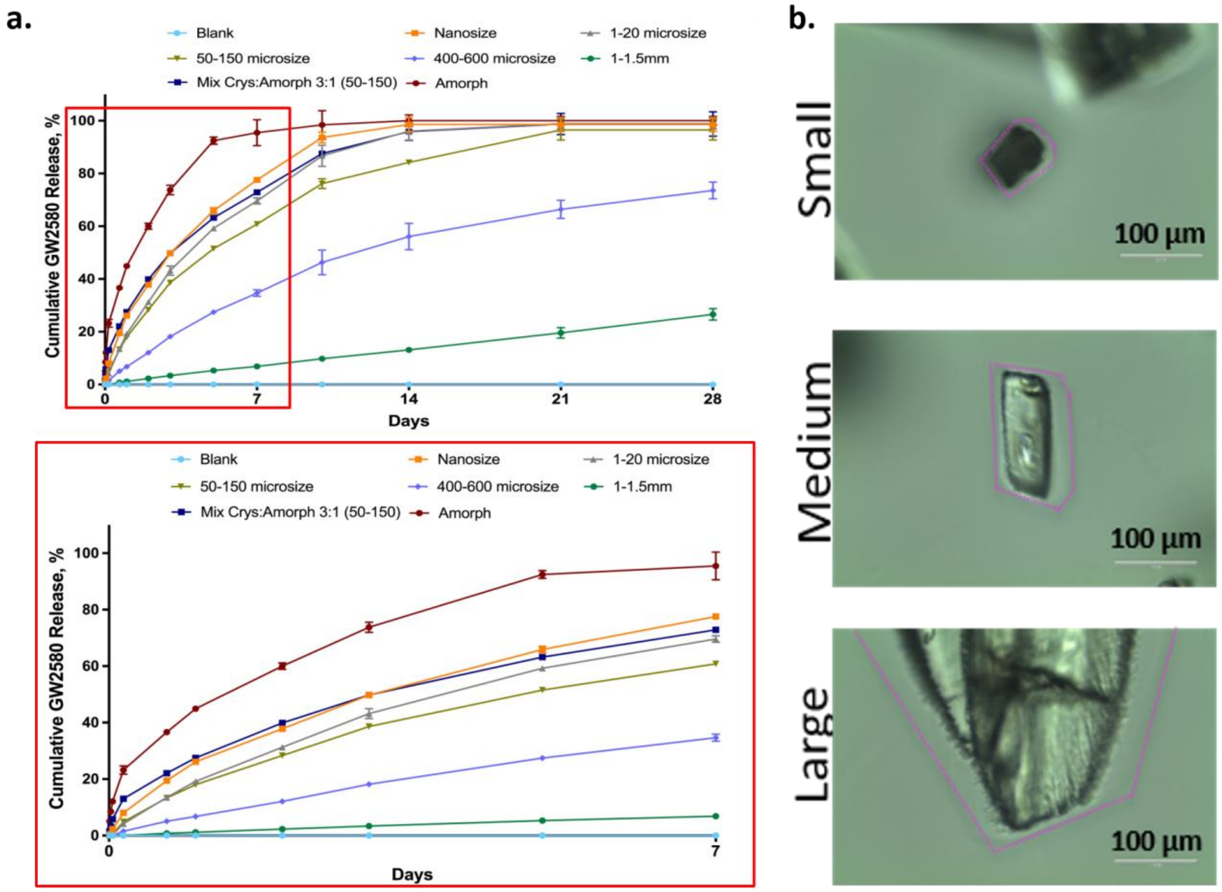

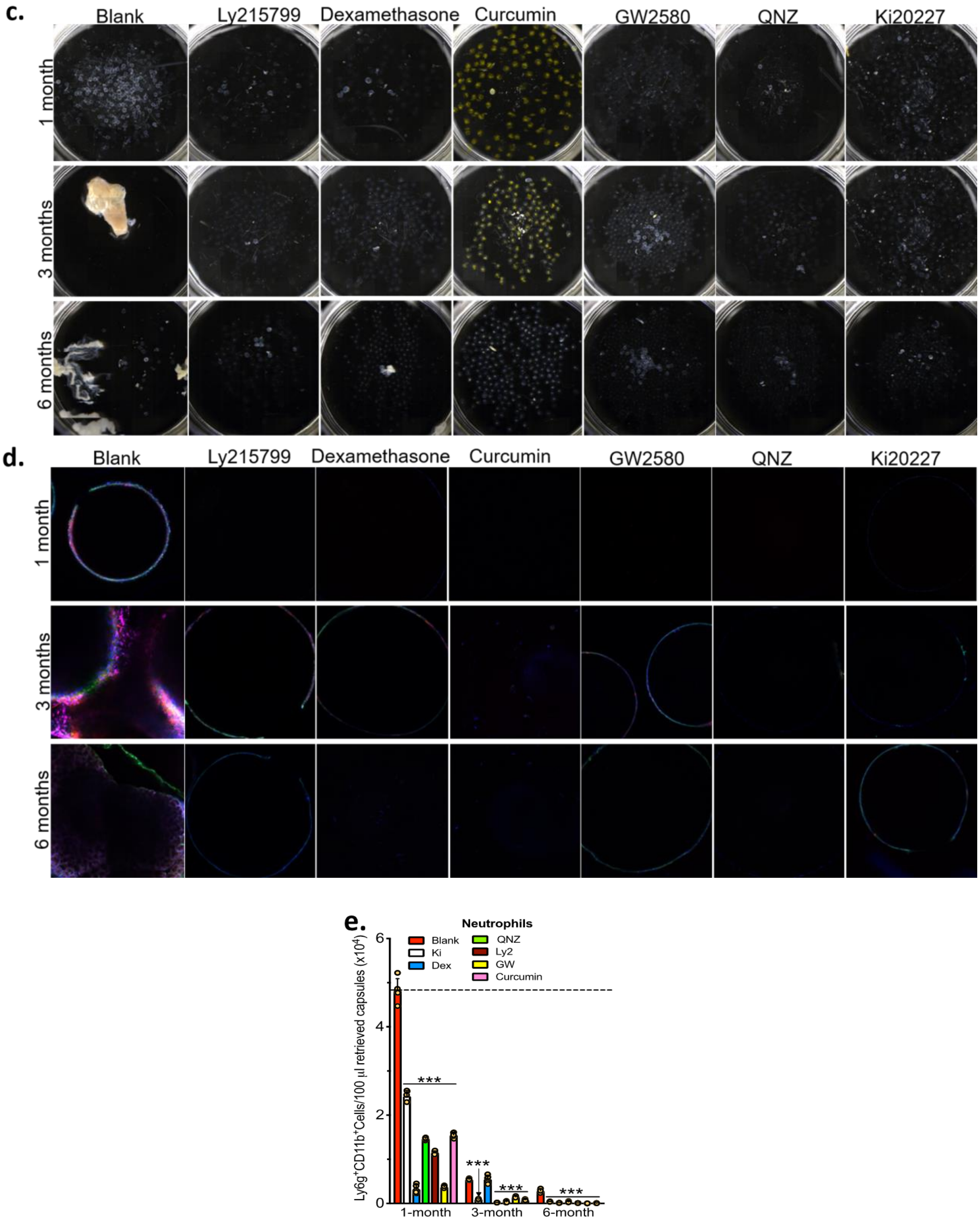

Supplemental Figure 10. In vitro release and in vivo anti-fibrotic efficacy testing in alginate in B6 mice – a) *In vitro* measurement of release under accelerated release conditions (37ºC, PBS + 0.1% SDS) for GW2580 encapsulated within 2000 μm alginate capsules. The full graph is a re-shown and corresponds to Fig. 3a, while the *zoom-in of graph highlight the first 7 days of the* *study*. Faster release was achieved with its encapsulated amorphous form (brown profile), while release from the crystalline formulations (different crystal size ranges, as specified) could be tuned by varying crystal size and the ratio of amorphous to crystalline and to a range of rates. Mean +/- SD. **b**) Microscope images following release of GW2580 (GW) crystalline (small, medium, and large formulations) loaded into alginate capsules. All crystal sizes eventually leave behind empty spaces within the crosslinked 3D alginate. Original crystal dimensions: pink dashed line. **c**) Phase contrast images showing host foreign body response (immune cell adhesion and fibrosis), observed as yellowish-white plaque on the otherwise translucent alginate microspheres. A number of anti-inflammatory agents (as indicated) as crystalline formulations encapsulated in ~500 μm alginate spheres showed significant long-term anti-fibrotic efficacy after 1, 3, and 6-month IP implantations in C57BL/6 mice (N = 5/group). Note: drug crystals have a colored appearance, making the crystalline drug loaded-alginate capsules more opaque in appearance (ie., orange-yellow for curcumin, white for GW). **d**) Confocal microscopy images showing reduced or no fibrotic overgrowth with crystalline-formulated drugs encapsulated in implanted alginate microspheres (Blue, DAPI nuclear stain; Green: Macrophage CD68; and Red: Fibrosis marker α-smooth muscle actin). **e**) Quantitative FACS analysis performed on cells dissociated directly off of alginate spheres, retrieved after various IP implantation times. All subpanels reflect representative data from experiments repeated 3 times.

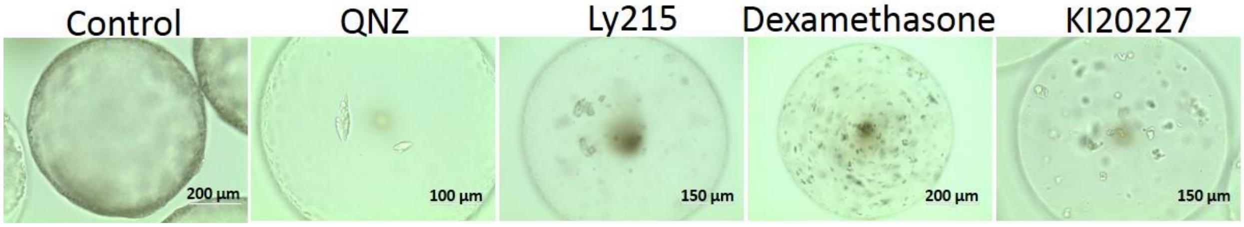

Supplemental Figure 11. Microscopy evaluation of retrieved capsules following 6 months in vivo implantation – Representative light microscope images of ~500 μm alginate capsules loaded with leading drug crystals retrieved after 6-month incubations in the IP space of C57BL/6 mice (N = 5/group) as compared to blank capsule controls (corresponding to the long-term study in Fig. 3). Capsules loaded with crystals were found to be free of fibrosis and remaining crystals were identified with darker crystalline particles especially the one located at the center of the capsules. Subpanel reflect representative data from experiments repeated 3 times.

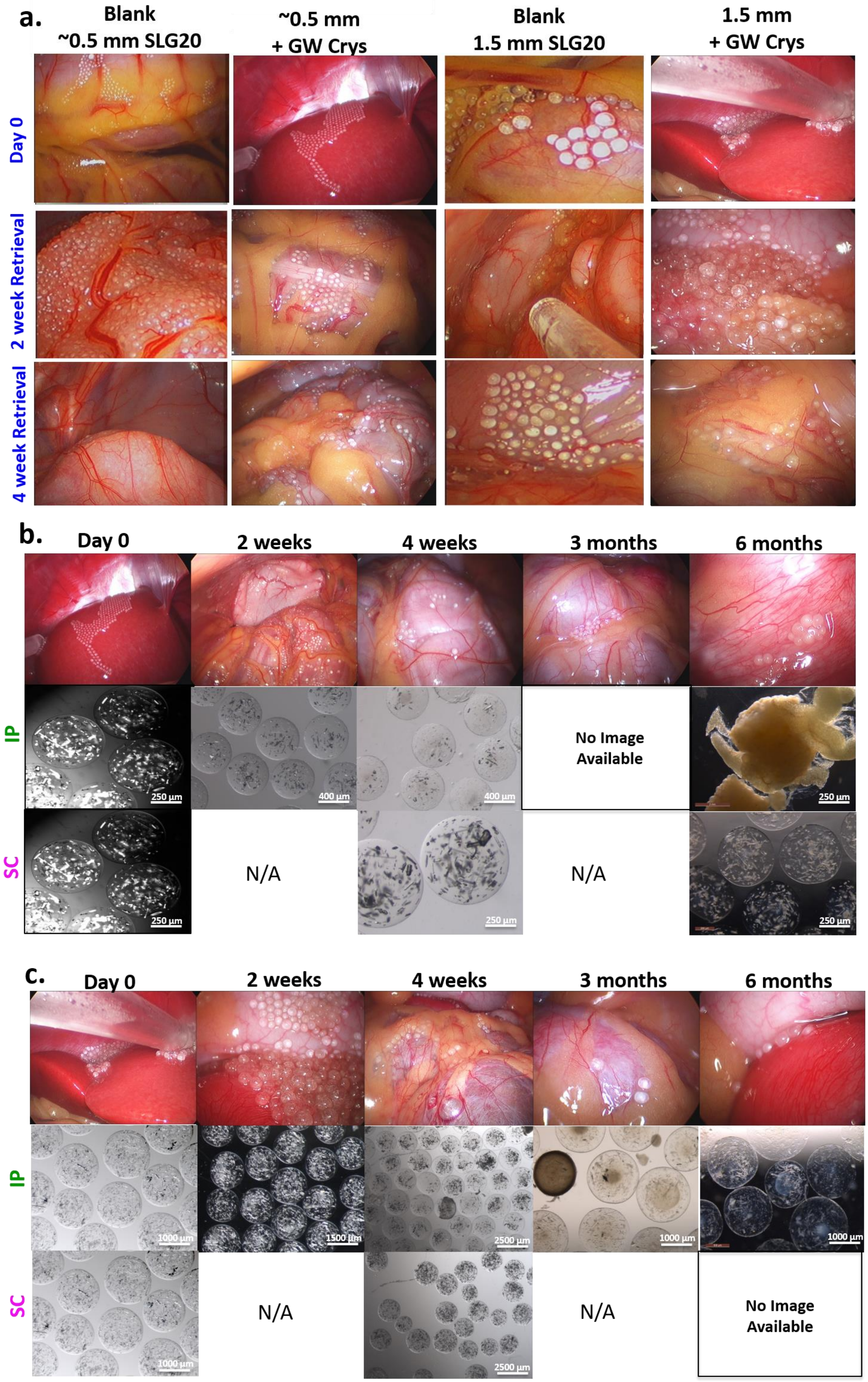
a.
Blank
~0.5 mm SLG20
~0.5 mm
+ GW Crys
Blank
1.5 mm SLG20
1.5 mm
+ GW Crys
Day 0
2 week Retrieval
4 week Retrieval
b.
Day 0
2 weeks
4 weeks
3 months
6 months
IP
SC
250 µm
400 µm
400 µm
No Image Available
250 µm
250 µm
N/A
250 µm
N/A
250 µm
c.
Day 0
2 weeks
4 weeks
3 months
6 months
IP
SC
1000 µm
1500 µm
2500 µm
1000 µm
1000 µm
1000 µm
N/A
2500 µm
N/A
No Image Available

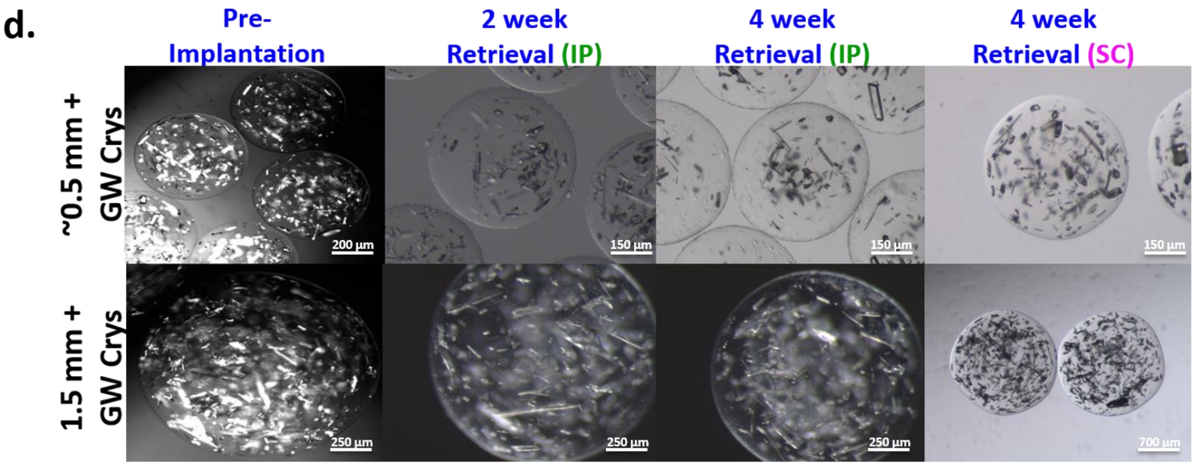
d.
Pre-Implantation
2 week Retrieval (IP)
4 week Retrieval (IP)
4 week Retrieval (SC)
~0.5 mm + GW Crys
1.5 mm + GW Crys
200 µm
150 µm
150 µm
150 µm
250 µm
250 µm
250 µm
700 µm

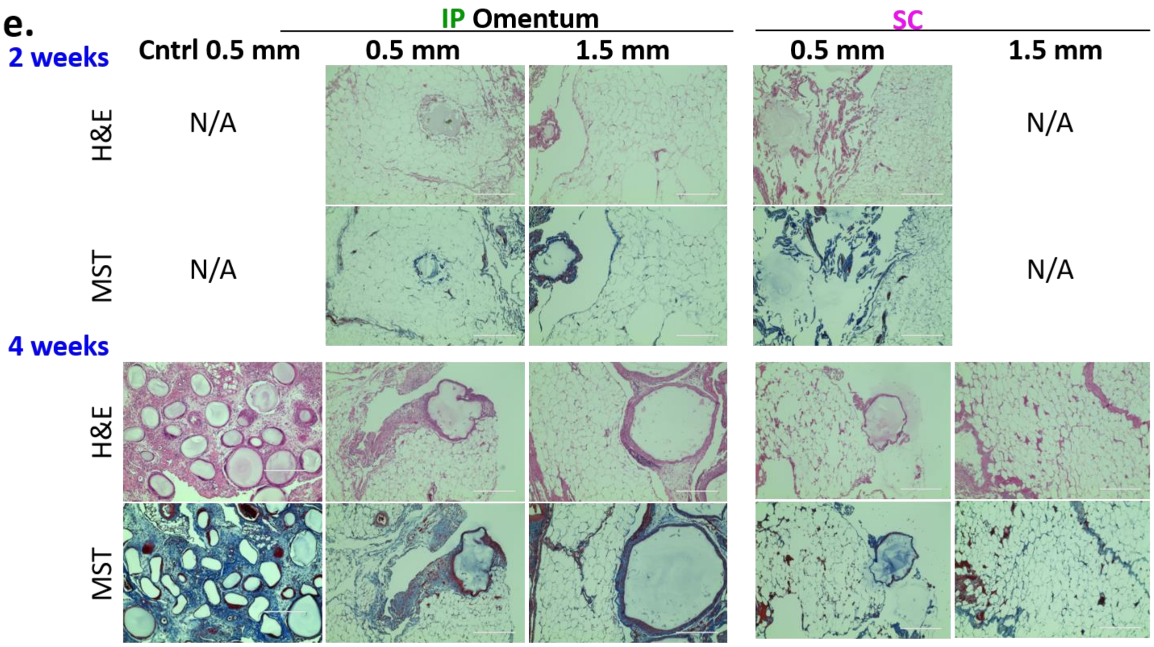
e.
IP Omentum
SC
2 weeks
Cntrl 0.5 mm
0.5 mm
1.5 mm
0.5 mm
1.5 mm
H&E
N/A
N/A
MST
N/A
N/A
4 weeks
H&E
MST

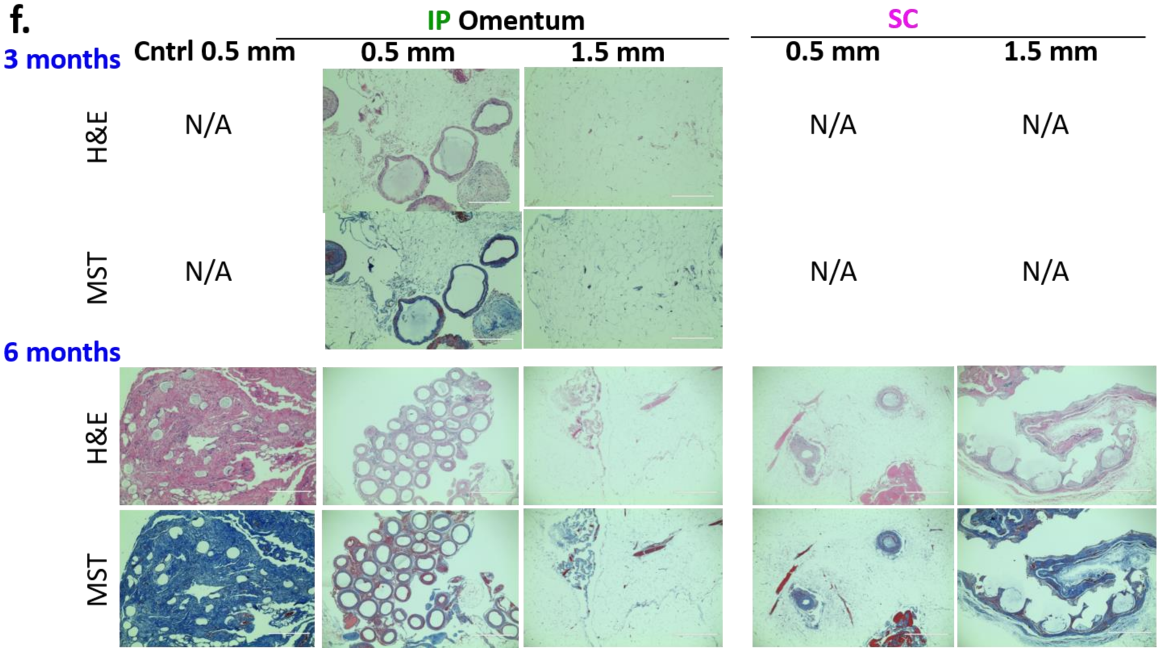
f.
IP Omentum
SC
3 months
Cntrl 0.5 mm
0.5 mm
1.5 mm
0.5 mm
1.5 mm
H&E
N/A
N/A
N/A
MST
N/A
N/A
N/A
6 months
H&E
MST

Supplemental Figure 12. Laparoscopic evaluation of implanted capsules in non-human primates – a) Laparoscopic images showing host foreign body response (loss of resolution and increasing cellular and tissue overgrowth) against 0.5 and 1.5 mm diameter alginate spheres encapsulating no drug (1st and 3rd columns) or crystalline CSF1R inhibitor GW2580 (2nd and 4th columns), on the day of implantation (Day 0) or after 2 and 4 week implantations, respectively, in the intraperitoneal (IP) space in non-human primates (NHP); N = 2/group. Note: drug crystals have a colored appearance, making the crystalline drug loaded-alginate capsules more opaque in appearance (white for GW2580). Laparoscopic and/or phase contrast images showing host foreign body response (immune cell adhesion and fibrosis) against 0.5 (**b**) and 1.5 mm (**c**) diameter alginate spheres encapsulating crystalline CSF1R inhibitor GW2580 on day 0, or after 2-week, 4-week, 3-month, or 6-month implantations in either the IP or subcutaneous (SC) space in non-human primates (NHP); N = 2/group. N/A, not applicable (not done). Not retrievable, indicates capsules were all overgrowth by this point in time, likely due to exhausted drug. **d**) Phase contrast (5-10X) and/or brightfield images taken of retrieved capsules (at specified times) showing relative loss of encapsulated crystal drug density for either 0.5 or 1.5 mm capsules (for drug extraction analysis see Fig. 4b). H&E and Masson's Trichrome stained histological sections of excised IP omentum or SC tissue at 2 and 4 weeks (**e**) or 3 and 6 months (**f**) post-implant showing reduced fibrosis in various crystalline drug groups, as compared to blank (no drug) control spheres (Scale bar = 400 µm (10X) or 1000 µm (4X), respectively). See Supplementary Video 2-3 for 4-week 0.5 mm capsule retrievals with and without drug. All subpanels reflect representative data from experiments repeated twice.

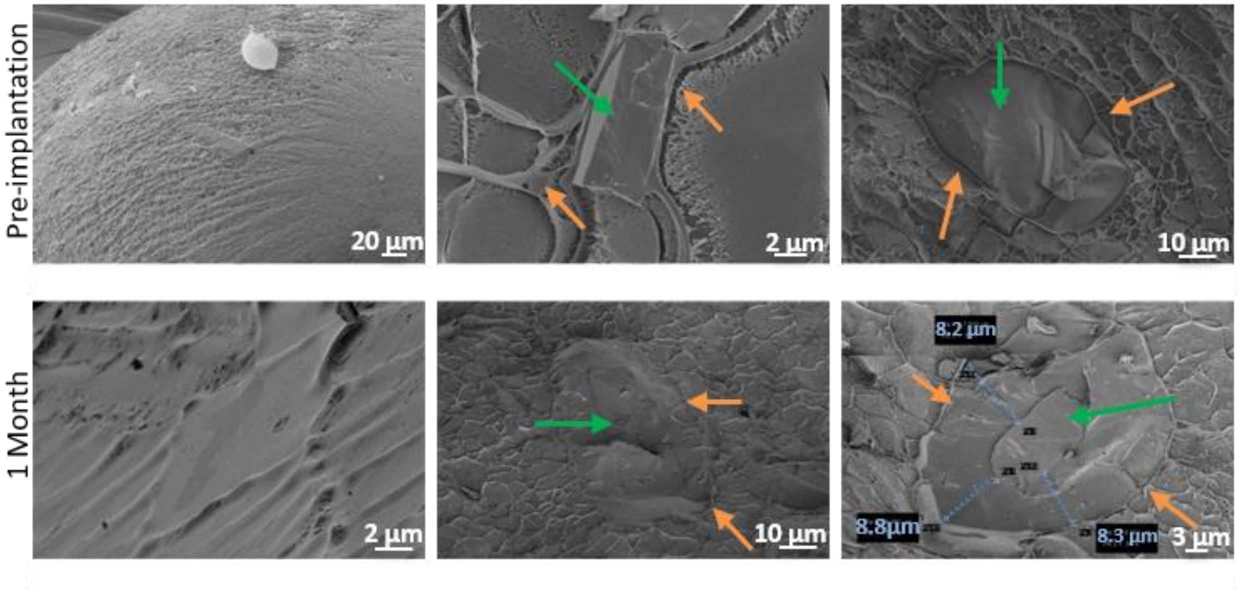

Supplemental Figure 13. Freeze-fracture cryo-SEM imaging of capsules pre and post implantation in non-human primates – 1.5 mm capsules loaded with crystalline GW2580 before or after being retrieved 1 month following IP implantation in NHP. Per time point: representative 1 capsule surface image and 2 freeze-fracture images, respectively, showing external and internal capsule-crystal organization. Inside the capsules, crystals marked with green arrows and surrounding polysaccharide is marked with orange arrows. Experiment run 3 times.

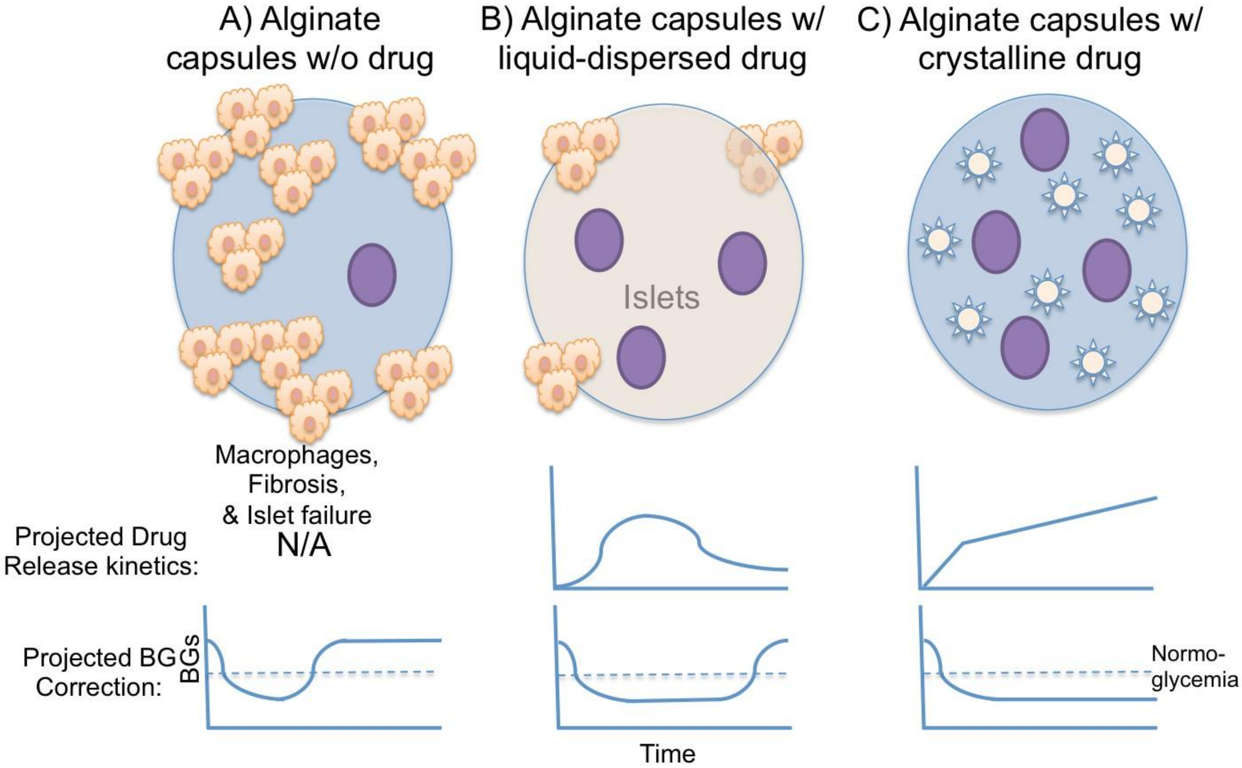

Supplemental Figure 14. Beta cells-drugs co-encapsulation strategy – Schematics showing varying fibrotic response and host rejection of implanted devices (i.e., alginate capsules bearing encapsulated islets for diabetes therapy) with either no co-encapsulated drug (**a**), liquid-dispersed/amorphous drug (**b**), or crystalline drug, capable of slower, yet elongated drug release kinetics (**c**), and their corresponding schematic graphs showing theoretical rates of drug diffusion and release and maintenance or loss of normoglycemia in diabetic subjects, depending on the drug reservoir.

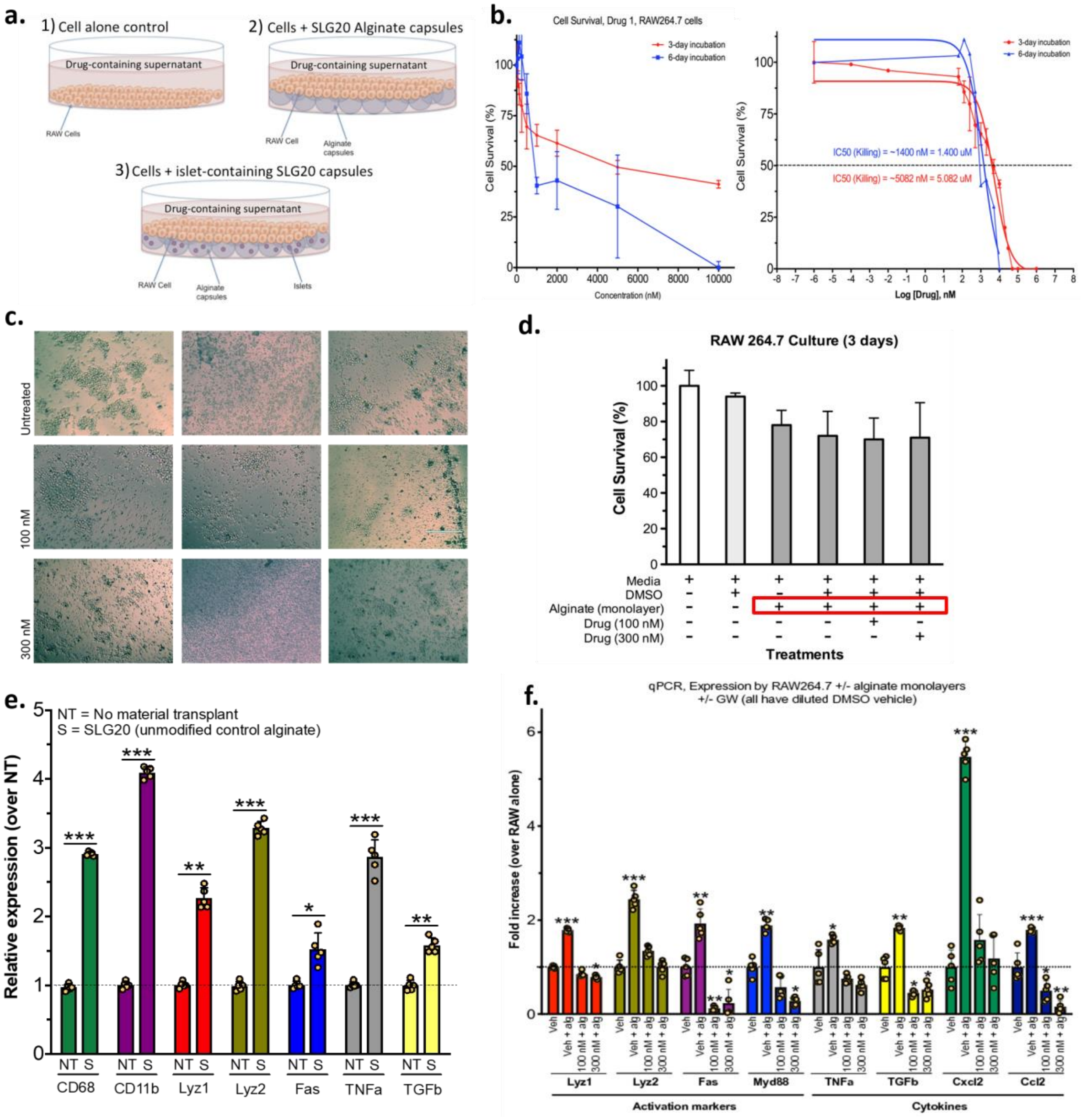

Supplemental Figure 15. In vitro evaluation drugs-macrophage cell line – a) Schematics showing in vitro culture incubations of seeded immortalized murine macrophage cell line RAW264.7 1) with or without drug, 2) with a present cross-linked spheres or monolayers of SLG20 alginate hydrogel (for induced material response), or 3) also with islets encapsulated within. **b**) IC_{50} curve generation for 3 and 6-day *in vitro* testing of drugs (in this case, Drug 1 = GW2580) for macrophage inhibitory capacity with the cell line RAW264.7. **c**) Photos showing seeded RAW264.7 cells on pre-crosslinked alginate monolayers in 96-well plate formats, showing no apparent cell density loss or toxicity with GW2580 at *in vitro* doses of 100 and 300 nM. **d**) CellTiter Glo results showing no GW2580 or DMSO vehicle toxicity to RAW264.7 cells.

There was, however, some slight residual barium (alginate crosslinker)-induced cell loss. **e**) Gene signatures (macrophage and inflammation) activated in primary macrophage and fibrosis responses in vivo in C57BL/6 mice following 2-week implantation. **f**) RAW cell *in vitro* signatures of some additional as well as the same genes (as shown in e), with cells alone (1st column), in the presence of alginate (2nd column), and when co-cultured with GW2580 (doses as specified, 3rd and 4th columns). Data: mean ± SEM, n = 5. Statistical analysis: one-way ANOVA with Bonferroni multiple comparison correction *: $p < 0.05$; **: $p < 0.001$, and ***: $p < 0.0001$; ns = not significantly different. All subpanels reflect representative data from experiments repeated 3 times.

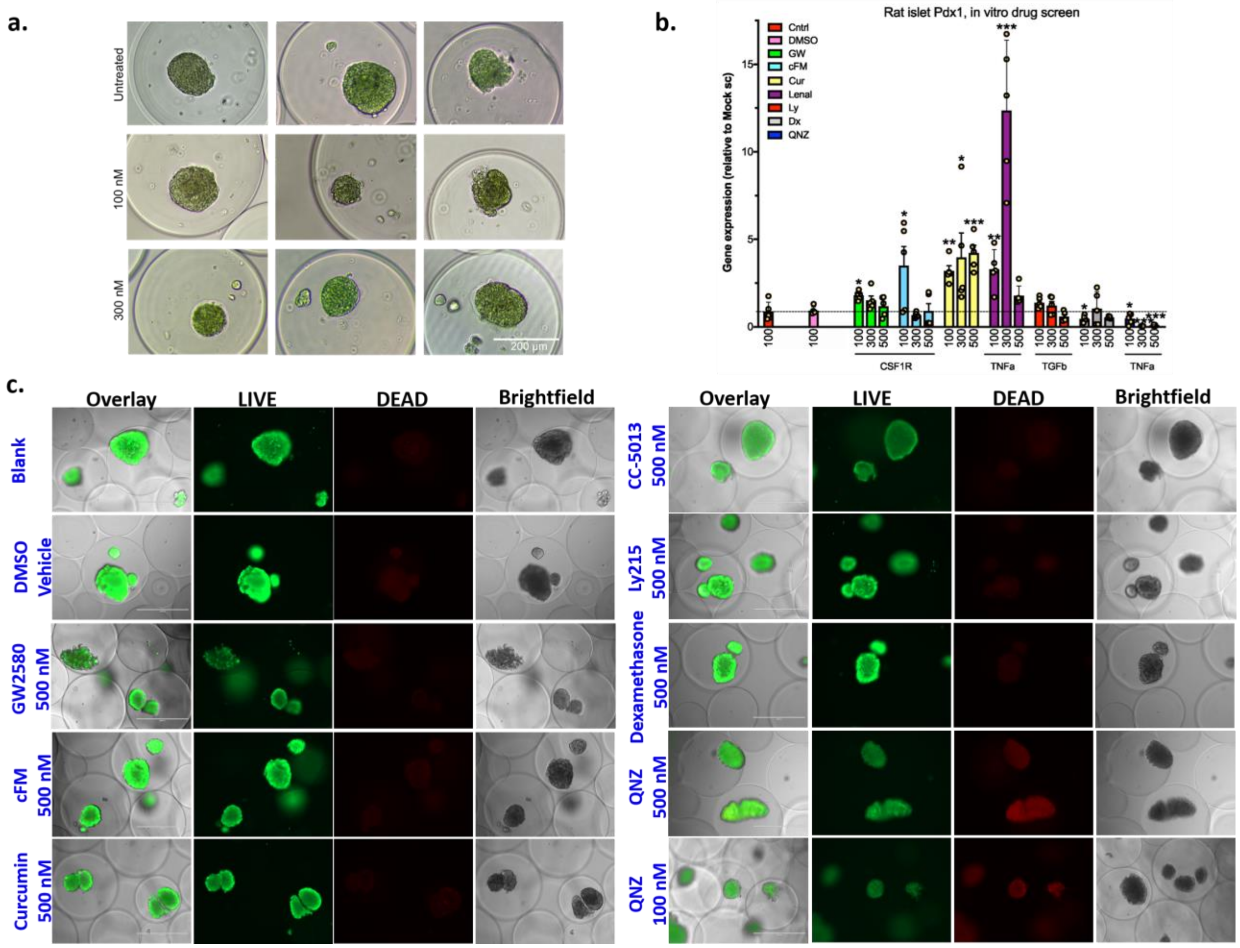

Supplemental Figure 16. In vitro drug safety screen for cell encapsulation – a) Drugs were tested and shown to be safe with no apparent toxicity to present rat primary islets, both in liquid-dispersed known and titered concentrations, as evidenced by healthy morphology (based on earlier IC$_{50}$ data, Supplementary Fig. 15). **b**) Islets were also assayed for the viability and functional marker Pdx1 after 2 days in culture in constant exposure to multiple drug concentrations (100, 300, & 500 nM), chosen from prior optimization of non-toxic doses necessary for prevention of RAW/Macrophage activation by alginate (Inhibition targets, along x-axis). In general, all drugs, other than QNZ, showed no toxicity to co-cultured encapsulated islets. **c**) LIVE/DEAD staining shows no apparent toxicity at tested in vitro drug doses for most drugs, again, except slight toxicity for QNZ. Data: mean ± SEM, n = 5. Statistical analysis: one-way ANOVA with Bonferroni multiple comparison correction *: $p < 0.05$; **: $p < 0.001$, and ***: $p < 0.0001$; ns = not significantly different. All subpanels reflect representative data from experiments repeated 3 times.

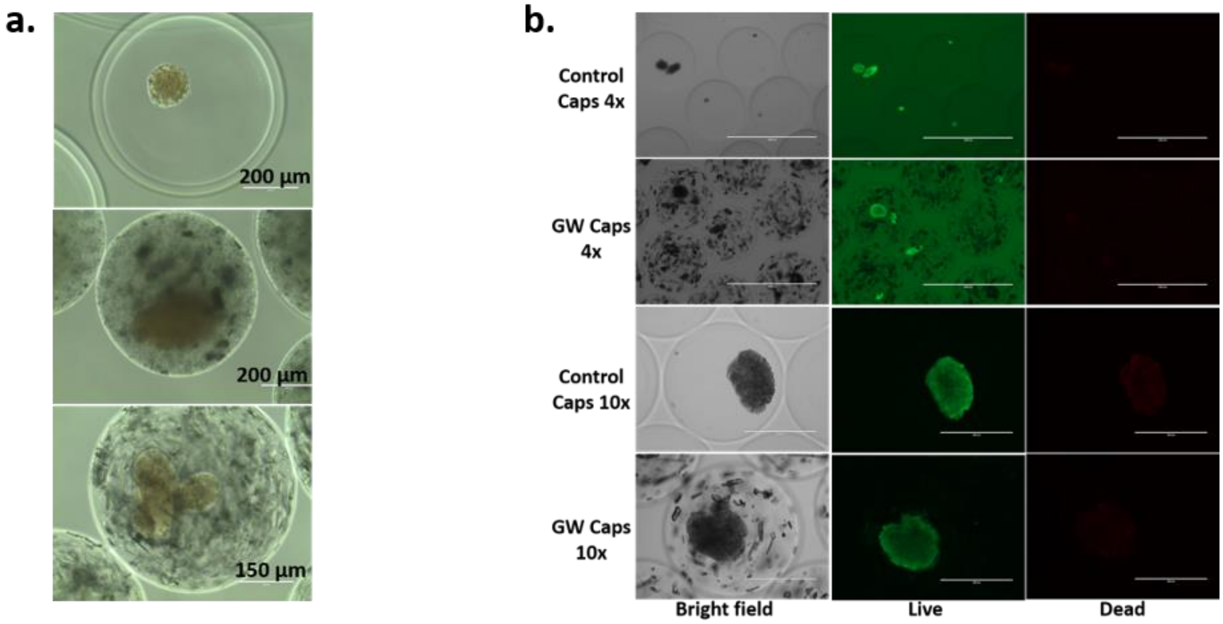

Supplemental Figure 17. Long-term glycemic control in STZ-C57BL/6 diabetic mice with crystalline GW2580 co-encapsulated with islets (rat or human) – a) Differential interference contrast (DIC) images of co-encapsulated crystalline GW2580 with rat islets; Scale bar = 200 µm or 150 µm, as indicated. **b)** Live/dead staining confirming viability of primary human islet clusters post-encapsulation for without or with crystalline GW2580 drug formulation prepared in ~500-600 µm-diameter alginate capsules, showing lack of cell toxicity. All subpanels reflect representative data from experiments repeated twice.

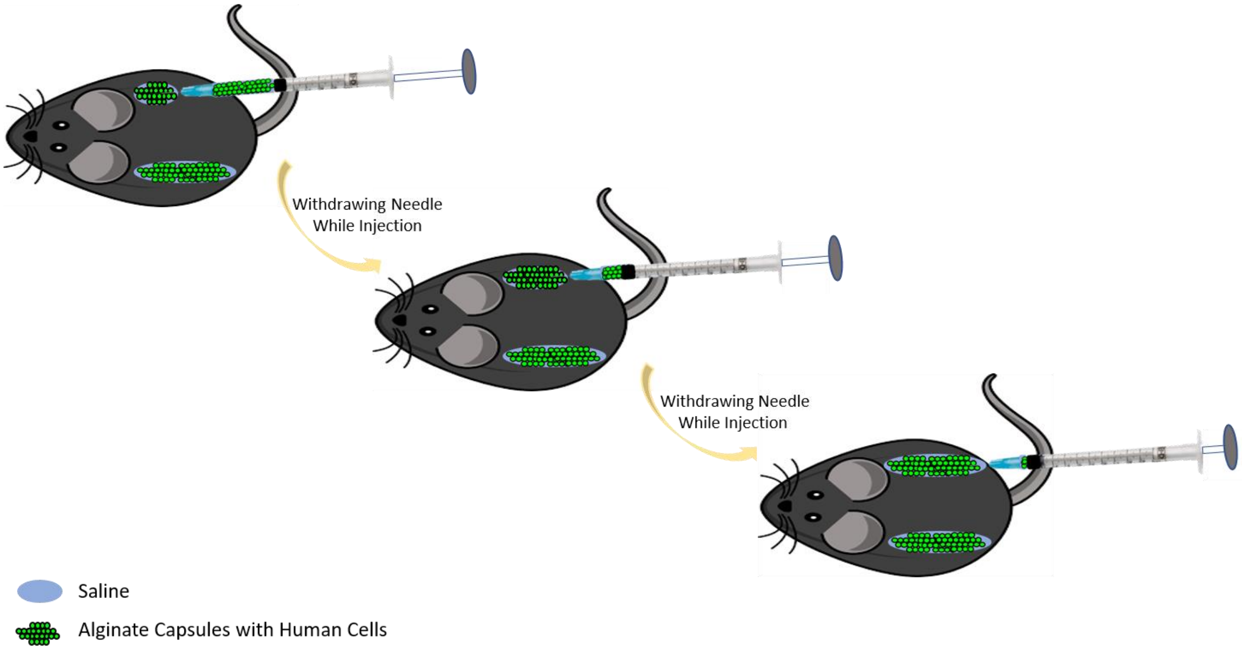

Supplemental Figure 18. Subcutaneous delivery by injection of human beta cells encapsulated in alginate capsules with/without GW2580 crystals – Capsules were placed in 2 separate but elongated subcutaneous locations, one on each side of the animal. Injection pockets were elongated by tunneling away from the needle stick site and injecting capsules continuously as the needle was slowly withdrawn. Experiment was repeated twice.

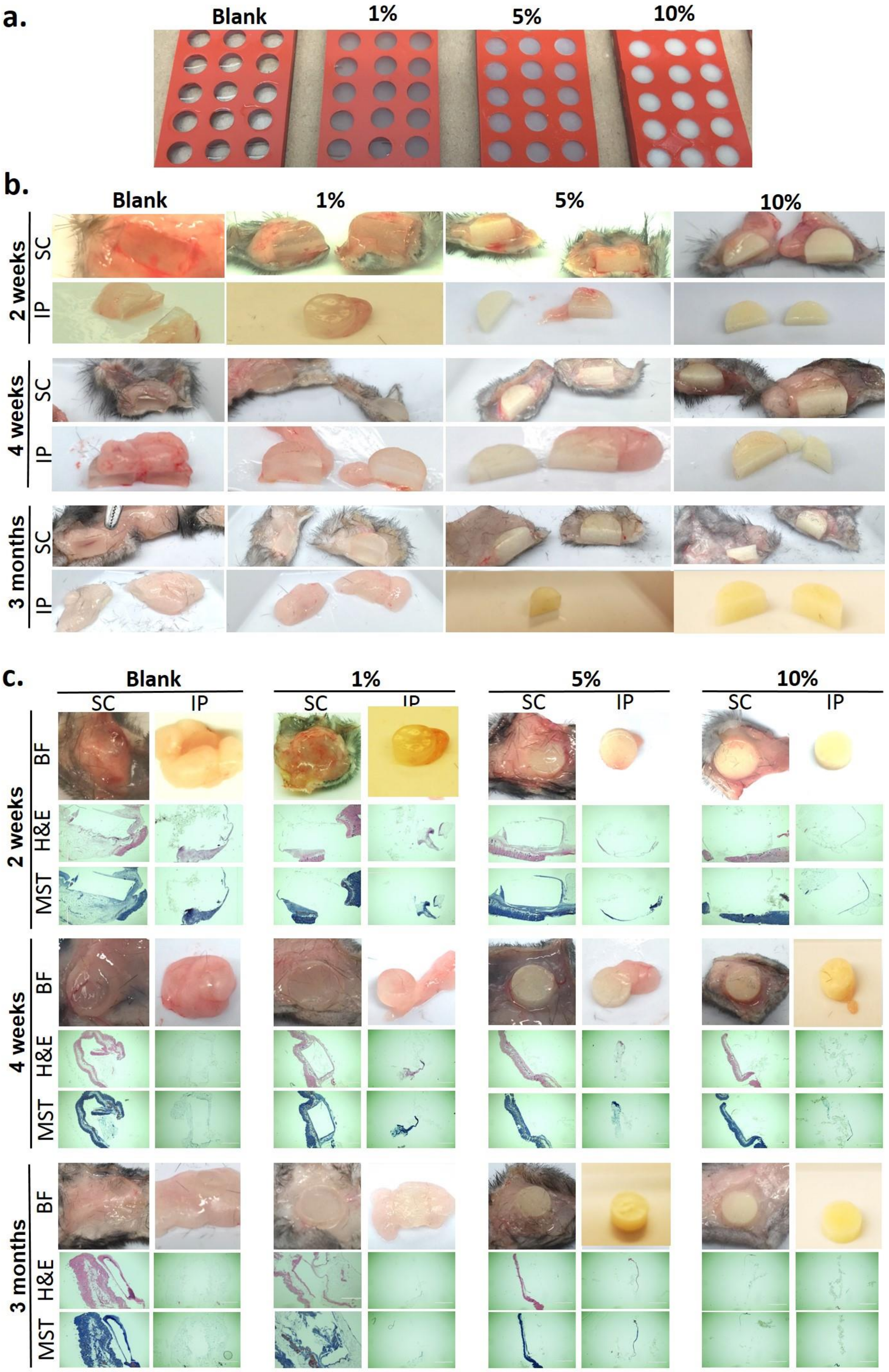
a.
Blank
1%
5%
10%
b.
Blank
1%
5%
10%
2 weeks
SC
IP
4 weeks
SC
IP
3 months
SC
IP
c.
Blank
1%
5%
10%
SC
IP
2 weeks
BF
H&E
MST
4 weeks
BF
H&E
MST
3 months
BF
H&E
MST

Supplemental Figure 19. PDMS discs fabrication and in vivo evaluation – a) *P*re-implant cured PDMS disc mold fabrication, showing photos of curing discs with no drug or with 1, 5, or 10% crystalline GW2580 (by weight). **b**) Additional images showing effective fibrosis inhibition with all drug-loaded PDMS discs after 2 weeks, 4 weeks, and 3 months post-IP or SC implantation in C57BL/6 mice (N=5/group). These images show a different point of view (than those in main Fig. 6h), after we took each implant we have cut it in half with downward compression of a razor blade, in order to cleanly capture a side view of the fibrotic overgrowth on implants over time. **c**) Images of H&E and Masson's Trichrome stained histological sections of excised SC and IP samples with tissue also at 2 and 4 weeks, in addition to the 3-month post-implant time point. Scale bar = 1000 µm; 4X. All subpanels reflect representative data from experiments repeated 3 times.

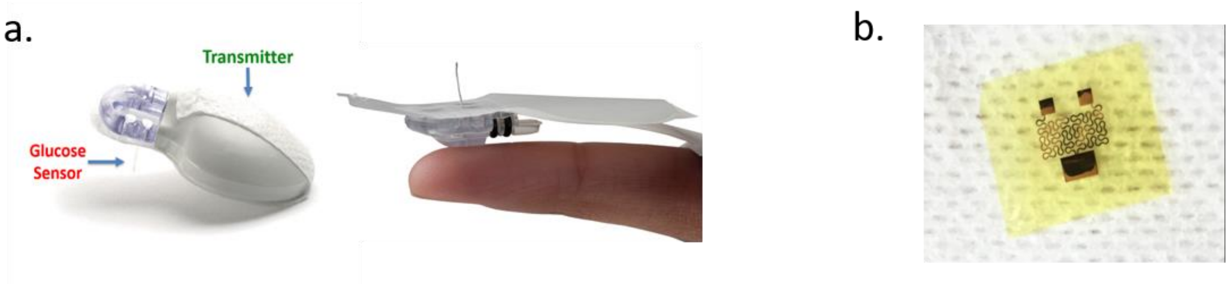

Supplemental Figure 20. Photos of multi-component devices used as two different models of implants with GW2580 crystals – a) Photo of continuous-glucose monitoring (CGM) Enlite sensor (second generation) for collecting blood glucose level. **b**) Photo of muscle stimulating device (MSD).

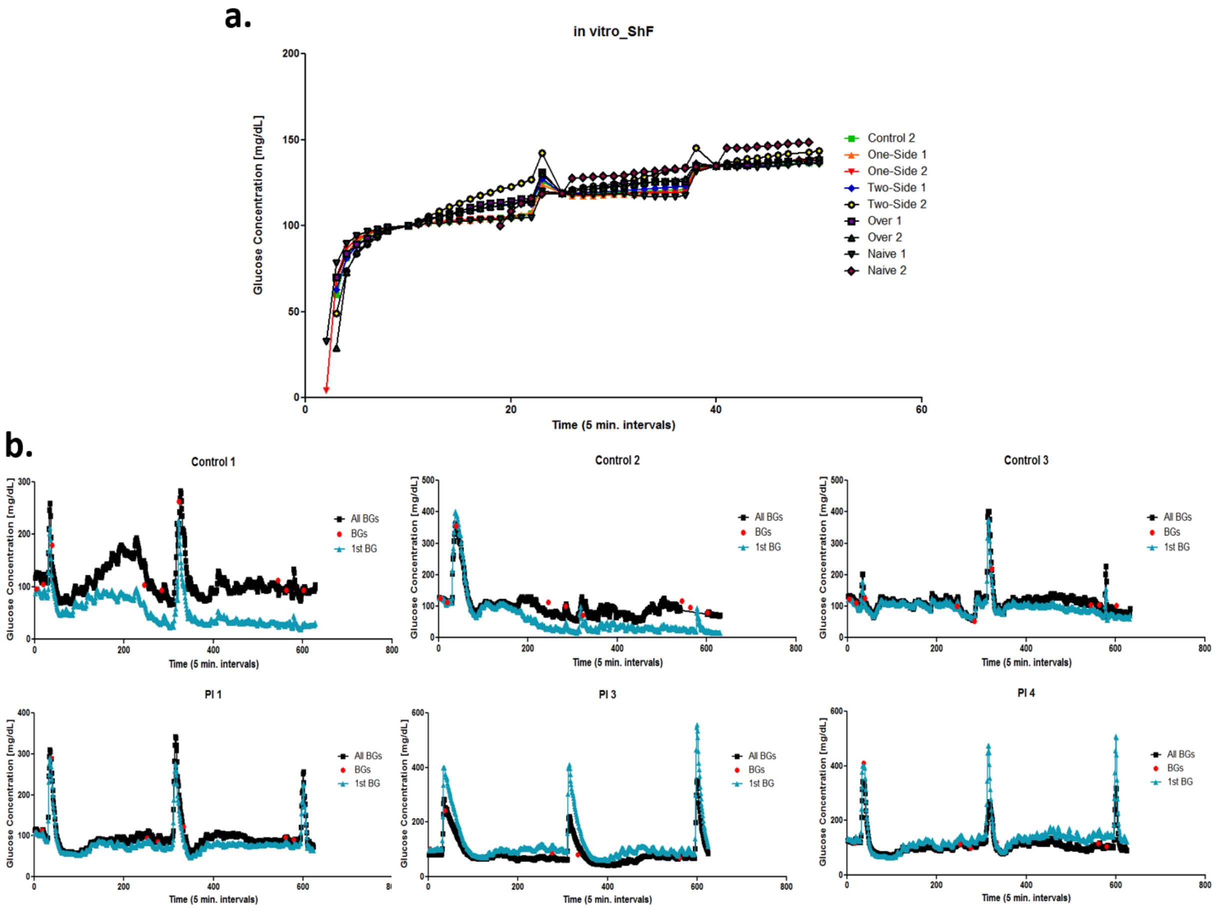

Supplemental Figure 21. In vitro and in vivo continuous-glucose monitor (CGM) functional testing – a) In vitro functional testing of CGM Enlite sensors (2nd generation) blank (control: stored at 37ºC in the same chamber as curing polyimide coated (PI) or Naive: stored at room temperature) vs PI coated on *1 side* (electrode side), *2 sides*, or *over* (over-loaded with 3 times the amount of PI used for 2-side coatings). No differences were found in the function of both coated and uncoated CGMs. Three days *in vivo* functional testing in SKH1 mice model for: **b**) uncoated CGMs vs **c**) CGMs coated with PI. No adverse effect was recorded due to sensor PI coatings; in contrast, an improvement was found where less background noise between the measured BG profile and calibrated sensor trend was observed. All subpanels reflect representative data from experiments repeated 3 times.

2) Supplementary Videos

Supplementary Video 1. *In situ* monitoring MII and MIII crystals stability and release with fluorescent microscope. Study was conducted under accelerated release conditions (37ºC, PBS +0.3% SDS) and monitored for 24h. Blackened crystals (MII, *upper*) were found to lose their structure/shape rapidly due to bulk release, as compared to MIII compact crystals (*lower*), which maintained their shape due to slow surface release. The video is representative for experiments repeated independently 3 times with similar results.

Supplementary Video 2. Laparoscopic evaluation and 4-week retrievals of implanted ~0.5 mm capsule without drug in non-human primates. The video is representative for experiments repeated independently twice with similar results.

Supplementary Video 3. Laparoscopic evaluation and 4-week retrievals of implanted ~0.5 mm capsule with GW2580 crystals in non-human primates. The video is representative for experiments repeated independently twice with similar results.

3) Supplementary Discussions:

1) *Crystals Thermal Stability*. Crystals from both techniques were examined for their thermal stability using differential scanning calorimetry (DSC) and thermogravimetric analysis (TGA) as compared to amorphous form **(Supplementary Fig. 3e)**. The amorphous formulation of GW2580 had a glass temperature (Tg) of 128°C and range of melting temperatures (Tm) around 209°C, indicating partial random self-crystallization during preparation. In comparison, crystals prepared by MII exhibited 2 peaks at 145°C and 189°C attributed to DMSO followed by crystal collapse and melting[47,48]. Crystals produced by crystallization MIII were found to have a single sharp Tm peak at 216.40°C indicating a pure fraction of compact crystals. Thermogravimetric curves of crystal sample mass change with temperature over the course of a pyrolysis reaction indicated a higher thermal stability of crystals from MIII. MII crystals exhibited early weight loss (18.9%), close to the calculated 17.6% DMSO content by SXRD.

2) *Details on the Mechanisms of Crystal Dissolution - Additional Details About the Formation of Dissolution Sites and Etch Pit Formation*. Prior etching studies observe the dissolution of single steps and the faceting of etch pits that match the overall morphology of the calcite crystals. Etch pits are known to form at local surface defects or at grain boundaries and are a common pathway for dissolution at crystal interfaces[65]. Counter to this dissolution studies[66] where they do not observe the formation of new dissolution sites; we observe the formation of single or double

crystallographic layer etch pits that result in layer-by-layer dissolution wherein the etch pits do not reflect the overall crystal morphology. This could be attributed to impurity incorporation into the crystalline lattice during crystal growth. The etch pits that form on F2 crystal surfaces are likely attributed to the incorporation of molecular level and macro-impurities during crystallization. Further, we do not observe etch pit morphologies that mirror the overall crystal habit, which have been observed for prior dissolution studies wherein etch pits for from line defects[67]. Due to the irregularity of the etch pits along the crystal surfaces (i.e., the etch pits do not form in aligned rows) and rounded pit morphologies, they are not likely related to line defects throughout the crystalline lattice.

For F2 (001) crystal surfaces, the molecular level impurities are observed during *in situ* AFM wherein the occluded atoms are released as evident by the monomolecular height etch pits. The larger etch pits result from macroscopy impurities being incorporated into the crystal lattice during growth and their release upon being exposed to solution. Both mechanisms are well known as a method for the crystal to relieve lattice strain which is induced by impurity incorporation which leads to misalignment of the atoms in the crystal lattice. Layer-by-layer dissolution from single step edges is the dominant method by which molecules are released from F2 crystals.

3) *Toxicity of Candidate Drugs to Islets*. Specifically, we sought to develop a technology useful for islet cell transplantation, and therefore examined the toxicity of candidate drugs to islets. Lead drugs from **(Fig. 1)** were screened for lack of toxicity, shown by CellTiter-Glo. Anti-fibrotic immunomodulatory capacity was then measured in vitro based on inhibition of fibrosis-associated gene expression upon material stimulation of immortalized murine macrophage RAW264.7 cells, alone or in combination with alginate prepared as monolayers **(Supplementary Fig. 15)**. Such in vitro profiles mirrored agent effects against primary macrophages in vivo **(Fig. 1)**. Leading candidates were also tested in vitro on encapsulated rat islets to study the potential for impact on islet biology and function, as we wanted to ensure that any targeted drugs chosen for crystallization and co-encapsulation in close proximity to islets would not be detrimental to their function and overall therapeutic efficacy **(Supplementary Fig. 16)**. Only one drug, QNZ, induced cellular toxicity at the concentrations tested **(Supplementary Fig. 16c)**.

4) *Polyimide with Crystals as Top Coating*: In both CGMs and MSDs cases, drug crystals were added into viscous polyimide (PI, fast curable polyamic acid) and applied as top coatings onto the implantable part of each device. PI has been used with medical devices previously due to coating properties and fast thermo-curing[55]. For CGMs, GW2580 and dexamethasone, crystals were prepared and applied with PI on the sensor electrode and thermo-cured. The effects of PI coatings on CGM sensor function were examined in vitro and in vivo (Supplementary Fig. 21). No reduction in the sensitivity was recorded while less background noise was found in vivo as compared to control uncoated CGMs (Supplementary Fig. 21b).

4) Supplementary References

65. Schreiber A, Rosenkranz C, Lohrengel MM. Grain-dependent anodic dissolution of iron. *Electrochimica Acta* 2007, **52**(27)**:** 7738-7745.

66. Hillner PE, Manne S, Gratz AJ, Hansma PK. AFM images of dissolution and growth on a calcite crystal. *Ultramicroscopy* 1992, **42–44**(Part 2)**:** 1387-1393.

67. Van Enckevort WJP, Van Der Linden WH. On the relation between etch pits or growth hillocks and dislocations on the (111) faces of potassium aluminium alum. *Journal of Crystal Growth* 1979, **47**(2)**:** 196-202.